Available online at www.sciencedirect.com
ScienceDirect
Comput. Methods Appl. Mech. Engrg. 415 (2023) 116227
Computer methods in applied mechanics and engineering
www.elsevier.com/locate/cma

Efficient multi-scale staggered coupling of discrete and boundary element methods for dynamic problems

Guilherme Barros[a,*], Andre Pereira[c], Jerzy Rojek[b], John Carter[a], Klaus Thoeni[a]

[a] *Centre for Geotechnical Science and Engineering, The University of Newcastle, 2308 Callaghan, Australia*
[b] *Institute of Fundamental Technological Research, Polish Academy of Sciences, Pawinskiego 5B, 02-106 Warsaw, Poland*
[c] *Institute of Computing, Fluminense Federal University, Rua Passo da Patria 156, Niterói 24210-240, Brazil*

Received 23 May 2023; received in revised form 28 June 2023; accepted 28 June 2023
Available online 19 July 2023

Abstract

This paper presents a novel and highly efficient approach for coupling the Discrete Element Method (DEM) and the Boundary Element Method (BEM) for time-domain simulations of dynamic problems, utilising multi-scale staggered time integration. While the DEM captures phenomena with discontinuous behaviours, such as fracturing and granular flow, the BEM excels in accurately modelling seismic wave propagation in infinite domains. By separately solving the governing equations of the DEM and BEM at different time instants, the proposed scheme considerably enhances computational efficiency compared to conventional monolithic coupling schemes. The incorporation of non-conforming interfaces enables larger time steps in the BEM, thereby reducing computational costs and memory usage. Moreover, an innovative coupling of DEM rotations with the BEM displacement field is introduced, leading to more accurate and realistic modelling of complex dynamics. Numerical experiments are conducted to demonstrate the superior accuracy and efficiency of the proposed method, establishing its potential for modelling a wide range of dynamic problems.

Keywords: BEM-DEM coupling; Multi-scale time integration; Rotational degrees of freedom; Seismic wave propagation; Infinite domain; Computational efficiency

1. Introduction

Numerical simulations have become an indispensable tool in geotechnical engineering and rock mechanics, allowing engineers and researchers to better understand complex soil and rock behaviour under various loading and environmental conditions [1,2]. The DEM and the BEM are among the widely employed numerical methods for performing these simulations. These methods have been used in a myriad of problems such as earthquakes [3,4], ballistic impacts [5], blasting processes [6–8], excavations [9,10], rock cutting [11], slope stability analysis [12,13], soil–structure interaction [14,15], tunnelling [16–18], and foundation design [19,20].

The DEM excels in simulating complex material behaviours and geometrical non-linearities [21]. It is a particle-based method that models an assembly of particles interacting via contact forces, making it suitable for simulations

* Corresponding author.
E-mail address: guilherme.coelhogomesbarros@uon.edu.au (G. Barros).

https://doi.org/10.1016/j.cma.2023.116227

at micro- and meso-scales [22]. The original formulation was later extended to model cohesive materials, such as rock or concrete, by incorporating new contact laws [23]. However, one limitation of the DEM is its difficulty in handling unbounded domains, often required in geomechanics [24]. This can be mitigated through non-reflecting viscous boundary conditions [25] or infinite elements [26], but these techniques do not allow for simulating wave propagation outside the computational domain.

On the other hand, the BEM is a continuum-based method that can accurately and efficiently model infinite domains [27]. The formulation utilises fundamental solutions that satisfy the radiation condition, allowing for eliminating domain integrals [28]. This results in a lower order of discretisation within the limits of elasticity. The BEM can model wave propagation towards infinity in elastodynamics [29,30] and solve a broader spectrum of problems, including viscoelasticity and poroelasticity, using the Convolution Quadrature Method (CQM) [31,32]. However, the BEM is unsuited for simulating complex material behaviours and geometrical non-linearities.

Although different numerical methods are appropriate for modelling specific physical phenomena within a particular domain and scale, real-life simulations often entail the simultaneous modelling of diverse phenomena at varying scales [33]. Therefore, it is common to combine different methods to create more comprehensive numerical models [34,35]. For instance, the DEM was coupled with several other methods to expand its modelling capabilities. The work of Oñate and Rojek [36] introduced a contact law between DEM particles and the edge of the elements in the Finite Element Method (FEM), being among the first to couple the DEM with a continuum-based method. Later, Azevedo and Lemos [37] introduced the interface FEM-DEM coupling. Rojek and Oñate [38] identified spurious wave reflections on the interface and proposed an overlapping domain coupling, extending the work of Xiao and Belytschko [39]. Simultaneously, Bauman et al. [40] developed a similar approach called the Arlequin coupling. Particle rotations were included in the coupling through the overlapping domain in [41,42]. More recently, efficient adaptative FEM-DEM frameworks were developed [34,43–45].

The BEM has also been coupled with the FEM to extend its modelling capabilities [46]. Most of early BEM-FEM models considered static problems [46–48]. The work of von Estorff and Prabucki [49] pioneered this coupling in transient problems in the time domain using the Newmark method to eliminate FEM velocities and accelerations. The work of Soares et al. [50] improved the efficiency of the coupled solution by truncating the BEM convolution. A study by Moser et al. [15] utilised Duhamel integrals to obtain a dynamic stiffness matrix for the BEM and combined it with the FEM to simulate soil–structure interaction. Similarly, Rüberg and Schanz [51] used the CQM-BEM in conjunction with FEM to solve non-conforming interfaces using a Lagrangian approach. François et al. [52] introduced an iterative coupling method that permits different time discretisation in every subdomain.

Although the DEM and the BEM have shown promising results on their own and in combination with other methods, there have been few attempts to harness their combined capabilities. Burczynski et al. [53] coupled the BEM with Molecular Dynamics for static analyses, while Mirzayee et al. [54] presented a coupling between the Distinct Element Method and the BEM in the frequency domain. However, existing works on the coupled BEM-DEM in the time domain are limited to quasi-static simulations due to the application of the static formulation of the BEM [55,56]. To the authors' best knowledge, the work of Malinowski et al. [57] was the first attempt to analyse dynamic problems in the time domain using the BEM and the DEM, but their results relied on a FEM layer and did not present a direct BEM-DEM coupling.

In a recent study, Barros et al. [58,59] investigated the monolithic coupling of BEM and DEM in the time domain for one- and two-dimensional problems. This approach couples the particle centre to the BEM node, leading to a boundary with excessive discretisation, which is computationally expensive. Furthermore, since a monolithic time integration is used, the time step size must be the same for both methods. However, the DEM and the BEM have different time step requirements, and this makes it challenging to find a single time step that ensures numerical stability for both methods. Moreover, the formulation does not couple the rotational DOFs of the interface, assuming no significant rotation in the far field.

This paper presents a new multi-scale time-staggered approach for coupling the DEM and the BEM. The method addresses the limitations of previous BEM-DEM formulations, such as an excessive number of unknowns and numerical instability. The multi-scale time staggered scheme allows for varying time steps, simplifying usage in real-world scenarios. The time step of the BEM is closely related to the element length, resulting in limitations on the time step when conforming interfaces are used. Therefore, this paper introduces non-conforming interface conditions to enhance the performance of the coupled solution. Furthermore, by integrating the coupling of rotations, the new approach allows for more realistic simulations.

This paper is structured as follows. Section 2 presents a background on the governing equations of the DEM and the BEM. Section 3 introduces the compatibility equations for the non-conforming interface and coupling of the rotational DOF. Section 4 discusses the time integration of the interface motion using the monolithic and staggered approaches. In Section 5, numerical examples demonstrate how the proposed method enhances accuracy and computational efficiency compared to existing methods. Finally, Section 6 covers the concluding remarks.

2. Governing equations

2.1. Discrete Element formulation

The current work uses the DEM to represent bodies as an assembly of two-dimensional circular particles (*i.e.* cylinders). In the DEM, Newton's law of motion governs the translations and rotations of each particle p as [22]

$$m_p \ddot{\boldsymbol{u}}_p = \boldsymbol{f}_p(t) \,, \tag{1}$$

$$\mathcal{J}_p \dot{\omega}_p = \mathcal{M}_p(t) \,. \tag{2}$$

In Eqs. (1) and (2), m_p and $\mathcal{J}_p$ are the mass and inertia of particle p, while $\ddot{\boldsymbol{u}}_p$ and $\dot{\omega}_p$ are its linear and angular accelerations, respectively. $\boldsymbol{f}_p$ and $\mathcal{M}_p$ are the resultant force vector and moment acting on particle p. The resultant force and moment have a component that is externally applied and internal ones that depend on contact with other particles, *i.e.*,

$$\boldsymbol{f}_p(t) = \boldsymbol{f}_{\text{ext},p}(t) + \sum_{q \in \mathcal{I}_p} \boldsymbol{f}_{\text{cont},pq}(t) \,, \tag{3}$$

$$\mathcal{M}_p(t) = \mathcal{M}_{\text{ext},p}(t) + \sum_{q \in \mathcal{I}_p} \mathcal{M}_{\text{cont},pq}(t) \,, \tag{4}$$

where $\boldsymbol{f}_{\text{ext},p}$ and $\mathcal{M}_{\text{ext},p}$ are the external forces and moment applied to particle p and $\boldsymbol{f}_{\text{cont},pq}$ and $\mathcal{M}_{\text{cont},pq}$ are the forces and moment due to contact between particles p and q for each particle in the set $\mathcal{I}_p$ of particles in contact with p.

Eqs. (1) and (2) are solved numerically using the "leapfrog" method, a second-order symplectic time integration scheme [*e.g.* 60–62]. Within the DEM domain, time is discretised in a series of time steps so that $t^{(i+1)} = t^{(i)} + \Delta t_{\text{D}}^{(i)}$, where $i \in \mathbb{N}$ indicates the number of steps and $\Delta t_{\text{D}}^{(i)}$ the size of the ith time step. All other variables are similarly discretised in time, *e.g.* $\boldsymbol{u}_p\left(t^{(i)}\right) = \boldsymbol{u}_p^{(i)}$. According to the "leapfrog" method, the velocities and displacements of particle p are updated as

$$\ddot{\boldsymbol{u}}_p^{(i)} = \frac{\boldsymbol{f}_p^{(i)}}{m_p} \,, \tag{5}$$

$$\dot{\boldsymbol{u}}_p^{\left(i+\frac{1}{2}\right)} = \dot{\boldsymbol{u}}_p^{\left(i-\frac{1}{2}\right)} + \ddot{\boldsymbol{u}}_p^{(i)} \Delta t_{\text{D}}^{(i)} \,, \tag{6}$$

$$\boldsymbol{u}_p^{(i+1)} = \boldsymbol{u}_p^{(i)} + \dot{\boldsymbol{u}}_p^{\left(i+\frac{1}{2}\right)} \Delta t_{\text{D}}^{(i)} \,. \tag{7}$$

Similarly, the rotational motion is described as,

$$\dot{\omega}_p^{(i)} = \frac{\mathcal{M}_p^{(i)}}{\mathcal{J}_p} \,, \tag{8}$$

$$\omega_p^{\left(i+\frac{1}{2}\right)} = \omega_p^{\left(i-\frac{1}{2}\right)} + \dot{\omega}_p^{(i)} \Delta t_{\text{D}}^{(i)} \,, \tag{9}$$

$$\theta_p^{(i+1)} = \theta_p^{(i)} + \omega_p^{\left(i+\frac{1}{2}\right)} \Delta t_{\text{D}}^{(i)} \,, \tag{10}$$

where θ_p is the rotation of particle p. It should be noted that Eqs. (8)–(10) are valid for two-dimensional circular particles (*i.e.* cylinders) only. The explicit time integration is conditionally stable, *i.e.* the size of the time step is bounded by the critical time step, *i.e.*, $\Delta t_{\text{D}}^{(i)} \leq \Delta t_{\text{D,cr}}$, that depends on local stiffness and mass [63,64]. The contact force is decomposed in normal and tangential directions, $\boldsymbol{n}_{pq}^{(i)}$ and $\boldsymbol{s}_{pq}^{(i)}$, by

$$\boldsymbol{f}_{\text{cont},pq}^{(i)} = f_{n,pq}^{(i)} \boldsymbol{n}_{pq}^{(i)} + f_{s,pq}^{(i)} \boldsymbol{s}_{pq}^{(i)} \,, \tag{11}$$

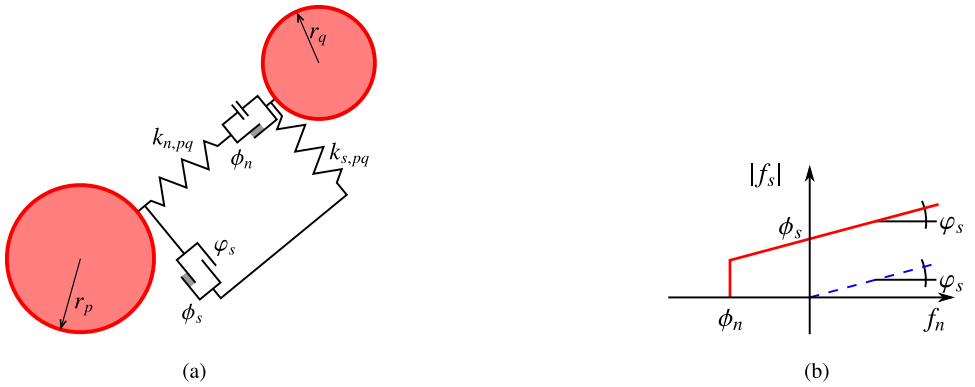

Fig. 1. Contact model: (a) rheological model and (b) Mohr–Coulomb law.

where, $f^{(i)}_{n,pq}$ and $f^{(i)}_{s,pq}$ are the normal and shear contact forces. The cohesive behaviour in the model limits these force components, following the Mohr–Coulomb law, by

$$f^{(i)}_{n,pq} \leq \phi_n \,, \tag{12}$$

$$f^{(i)}_{s,pq} \leq \phi_s - f^{(i)}_{n,pq} \tan\varphi_s \,, \tag{13}$$

where ϕ_n and ϕ_s are the normal and shear cohesions and φ_s is the friction angle. The Mohr–Coulomb law is depicted in Fig. 1(b), where the cohesive behaviour is shown as a solid red line and the behaviour after the break of the cohesive bond as a blue dashed line.

In the explicit DEM, the contact forces are calculated incrementally as a function of the relative displacements between particles, *i.e.*

$$f^{(i)}_{n,pq} = f^{(i-1)}_{n,pq} + k_{n,pq}\,\Delta\delta^{(i)}_{n,pq} \,, \tag{14}$$

$$f^{(i)}_{s,pq} = f^{(i-1)}_{s,pq} + k_{s,pq}\,\Delta\delta^{(i)}_{s,pq} \,. \tag{15}$$

where $k_{n,pq}$ and $k_{s,pq}$ are the normal and shear stiffnesses of the contact (*cf.* Fig. 1(a)), and $\Delta\delta^{(i)}_{n,pq}$ and $\Delta\delta^{(i)}_{s,pq}$ are the increments in the normal and tangential relative displacements [59]. As suggested in [60], the stiffnesses are defined based on the micro-mechanical Young's moduli $\tilde{E}_p$ and $\tilde{E}_q$, micro-mechanical Poisson's ratios $\tilde{\nu}_p$ and $\tilde{\nu}_q$ and radii r_p and r_q as

$$k_{n,pq} = 4\frac{\tilde{E}_p r_p \tilde{E}_q r_q}{\tilde{E}_p r_p + \tilde{E}_q r_q} \,, \tag{16}$$

$$k_{s,pq} = 4\frac{\tilde{E}_p r_p \tilde{\nu}_p \tilde{E}_q r_q \tilde{\nu}_q}{\tilde{E}_p r_p \tilde{\nu}_p + \tilde{E}_q r_q \tilde{\nu}_q} \,. \tag{17}$$

2.2. Boundary Element formulation

The BEM formulation is based on continuum mechanics. Betti's reciprocal theorem [30] states the reciprocity between the actual system and an infinite one where a point load (Dirac delta) is applied at a specific point and time. That allows the displacement in the original system to be calculated as

$$\boldsymbol{C}\boldsymbol{u} = \int_{\Gamma} \boldsymbol{U}^* \circledast \boldsymbol{t}\,\mathrm{d}\boldsymbol{x} - \int_{\Gamma} \boldsymbol{T}^* \circledast \boldsymbol{u}\,\mathrm{d}\boldsymbol{x} \,, \tag{18}$$

where $\boldsymbol{C}$ is a matrix containing jump terms derived from the Dirac delta integration, $\boldsymbol{u}$ and $\boldsymbol{t}$ are the displacement and traction vectors, respectively, and $\boldsymbol{U}^*$ and $\boldsymbol{T}^*$ are matrices containing the fundamental solutions of displacements and tractions, respectively. The fundamental solutions are the response at the field point $\boldsymbol{\xi}$ of an infinite medium under a point load applied at the source point $\boldsymbol{x}$ after a time t has elapsed. The symbol $\circledast$ represents a convolution integral [30].

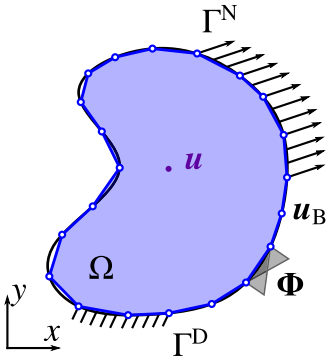

Fig. 2. The domain Ω discretised in boundary elements with Dirichlet and Neumann boundary conditions Γ^{D} and Γ^{N} respectively.

The displacement and traction fields are discretised over the boundary as

$$\boldsymbol{u}\left(\boldsymbol{x},t\right)=\boldsymbol{\Phi}\left(\boldsymbol{x}\right)\boldsymbol{u}_{\mathrm{B}}\left(t\right)\,, \tag{19}$$

$$\boldsymbol{t}\left(\boldsymbol{x},t\right)=\boldsymbol{\Psi}\left(\boldsymbol{x}\right)\boldsymbol{t}_{\mathrm{B}}\left(t\right)\,, \tag{20}$$

where $\boldsymbol{u}_{\mathrm{B}}$ is the nodal displacements vector, $\boldsymbol{t}_{\mathrm{B}}$ is the tractions vector, and $\boldsymbol{\Phi}\left(\boldsymbol{x}\right)$ and $\boldsymbol{\Psi}\left(\boldsymbol{x}\right)$ are their interpolating shape-functions, as shown in Fig. 2. The current work uses linear shape functions for $\boldsymbol{\Phi}$ and $\boldsymbol{\Psi}$. Substituting the space discretisation in Eq. (18), one may write

$$\boldsymbol{C}\boldsymbol{u}=\boldsymbol{G}\circledast\boldsymbol{t}_{\mathrm{B}}-\boldsymbol{H}\circledast\boldsymbol{u}_{\mathrm{B}}\,, \tag{21}$$

where

$$\boldsymbol{G}\left(\boldsymbol{\xi},t\right)=\int_{\Gamma}\boldsymbol{U}^{*}\left(\boldsymbol{\xi},\boldsymbol{x},t\right)\,\boldsymbol{\Psi}\left(\boldsymbol{x}\right)\,\mathrm{d}\boldsymbol{x}\,, \tag{22}$$

$$\boldsymbol{H}\left(\boldsymbol{\xi},t\right)=\int_{\Gamma}\boldsymbol{T}^{*}\left(\boldsymbol{\xi},\boldsymbol{x},t\right)\,\boldsymbol{\Phi}\left(\boldsymbol{x}\right)\,\mathrm{d}\boldsymbol{x}\,. \tag{23}$$

Note that, in Eq. (21), $\boldsymbol{u}_{\mathrm{B}}$ represents the nodal displacements of all DOFs at the boundary while $\boldsymbol{u}$ is the displacement of a point in the domain.

The CQM approximates the convolution integral in Eq. (21) utilising weighted summations. This results in a time-stepping numerical solution. Applying the CQM to Eq. (21) allows one to write [31]

$$\boldsymbol{C}\boldsymbol{u}=\sum_{k=0}^{j+1}\boldsymbol{G}^{(j+1-k)}\boldsymbol{t}_{\mathrm{B}}^{(k)}-\sum_{k=0}^{j+1}\boldsymbol{H}^{(j+1-k)}\boldsymbol{u}_{\mathrm{B}}^{(k)}\,. \tag{24}$$

This equation allows the calculation of displacements at any internal point once the displacements of the boundary are known. To calculate the displacements of the boundary, it is necessary to take the limit as this point tends to each of the boundary nodes. This process is known as collocation. By doing so, one may find

$$\sum_{k=0}^{j+1}\boldsymbol{H}_{\mathrm{B}}^{(j+1-k)}\boldsymbol{u}_{\mathrm{B}}^{(k)}=\sum_{k=0}^{j+1}\boldsymbol{G}_{\mathrm{B}}^{(j+1-k)}\boldsymbol{t}_{\mathrm{B}}^{(k)}\,. \tag{25}$$

The choice of the time step Δt_{B} is crucial to ensure numerical stability to the method. While a too-large time step leads to significant numerical damping, a too-small one requires the computation of large numbers that may overflow the floating point precision [31]. Therefore, the time step must be within a range, *i.e.*, $\Delta t_{\mathrm{B}}\in\left[\alpha\Delta t_{\mathrm{B,cr}},\beta\Delta t_{\mathrm{B,cr}}\right]$, where $0<\alpha<1$ and $\beta>1$ are real numbers. François et al. [52] suggest that $\alpha=0.7$ and $\beta=1.2$, but these values might be problem dependent. They also state that the critical time step $\Delta t_{\mathrm{B,cr}}$ can be estimated by,

$$\Delta t_{\mathrm{B,cr}}=\frac{L_e}{c_s}\,, \tag{26}$$

where L_e is the element length and c_s is the shear wave velocity of the material.

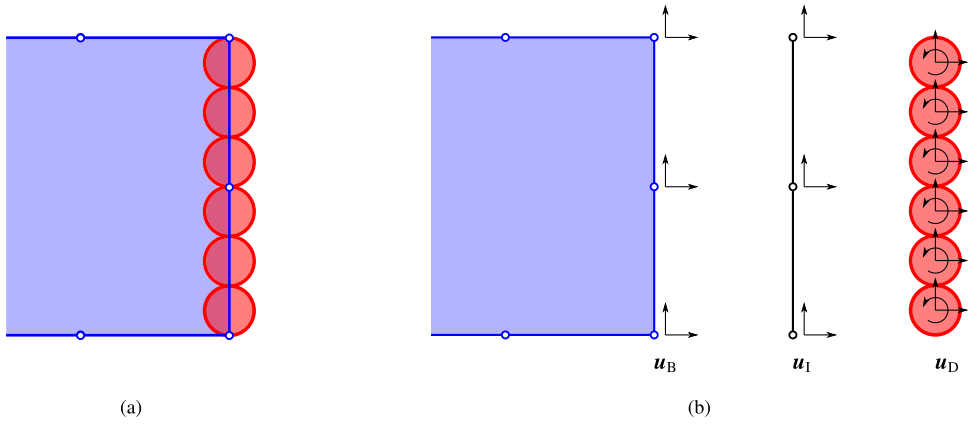

Fig. 3. Non-conforming BEM-DEM interface: (a) example of an arrangement of particles along the interface, and (b) DOFs of the BEM, the DEM, and the interface.

3. Compatibility equations at non-conforming interfaces

In the following section, the same instant for the BEM and the DEM is assumed, *i.e.*, $i\,\Delta t_{\mathrm{D}} = j\,\Delta t_{\mathrm{B}}$. The compatibility equations correlate the displacements of interface nodes $\boldsymbol{u}_{\mathrm{I}}$ with the displacements of particles and BEM nodes, as shown in Fig. 3. The interface's displacement field identically matches the displacement field of the BEM at the interface, *i.e.*,

$$\boldsymbol{u}_{\mathrm{B}} = \boldsymbol{u}_{\mathrm{I}}\,. \tag{27}$$

The displacements of particle p must be equal to the interface displacement at the same point. Therefore, if particle p has an initial position $\boldsymbol{x}_p^{(0)}$ which lies somewhere inside element $e$at the interface, the element's shape functions are used to write

$$\boldsymbol{u}_p = \boldsymbol{\Phi}_e\left(\boldsymbol{x}_p^{(0)}\right)\boldsymbol{u}_{\mathrm{I}}\,. \tag{28}$$

It is worth noticing that the matrix on the right-hand side of Eq. (28) contains shape functions of the Boundary Element (BE) evaluated at the particle's initial position and therefore does not vary with time, as long as small displacements are concerned.

Additionally, the rotation of the particle can be related to the rotation of the interface's displacement field, calculated by the curl of the vector field. In two dimensions, there is only one rotation around the z-axis, which is given by

$$\theta = \frac{\partial u_y}{\partial x} - \frac{\partial u_x}{\partial y} = \boldsymbol{\Omega}\boldsymbol{u}\,, \tag{29}$$

where

$$\boldsymbol{\Omega} = \begin{bmatrix} -\frac{\partial}{\partial y} & \frac{\partial}{\partial x} \end{bmatrix}. \tag{30}$$

Consequently, the rotation of particle p can be related to the interface's displacement field as

$$\theta_p = \boldsymbol{\Omega}\,\boldsymbol{\Phi}_e\left(\boldsymbol{x}_p^{(0)}\right)\boldsymbol{u}_{\mathrm{I}}\,. \tag{31}$$

This displacement field is piecewise continuous. Hence, the rotation of a particle located at an interface boundary element node is undetermined. To uniquely determine such rotation, one can take the average between the values provided by each two incident elements.

Then, the DOFs of the particles incident to the interface can be expressed in vector form as

$$\boldsymbol{u}_{\mathrm{D}} = (\boldsymbol{u}_0, \theta_0, \ldots, \boldsymbol{u}_P, \theta_P)\,. \tag{32}$$

Hence, one can assemble a system of constraint equations as

$$\boldsymbol{u}_{\mathrm{D}} = \boldsymbol{T}\boldsymbol{u}_{\mathrm{I}}\,, \tag{33}$$

where

$$\boldsymbol{T} = \left[\boldsymbol{\Phi}_{e_0}\left(\boldsymbol{x}_0^{(0)}\right), \boldsymbol{\Omega}\boldsymbol{\Phi}_{e_0}\left(\boldsymbol{x}_0^{(0)}\right), \ldots, \boldsymbol{\Phi}_{e_P}\left(\boldsymbol{x}_P^{(0)}\right), \boldsymbol{\Omega}\boldsymbol{\Phi}_{e_P}\left(\boldsymbol{x}_P^{(0)}\right)\right]. \tag{34}$$

Finally, one can take the second derivative with respect to time on both sides of Eq. (33) to write

$$\ddot{\boldsymbol{u}}_{\mathrm{D}} = \boldsymbol{T}\ddot{\boldsymbol{u}}_{\mathrm{I}}. \tag{35}$$

Both Eqs. (33) and (35) can be used to impose the condition that the movement of particles is restricted to the interface's admissible displacement field. They are equivalent because if the displacements are the same for all time, all their time derivatives will be equal. On the other hand, two functions with the same derivatives will differ at most by a constant factor corresponding to the problems' initial conditions. The choice between Eq. (33) or Eq. (35) depends on the type of time integration used. In the monolithic scheme, Eq. (33) has to be used because the BEM's final equation, Eq. (25), does not relate accelerations. In the staggered scheme, Eq. (35) can be used, which prompts a more straightforward framework.

The Betti–Maxwell reciprocal theorem states the equivalence of work between two elastic bodies. On the one hand, one can write the equivalence between the BEM and the interface as

$$\boldsymbol{u}_{\mathrm{I}}^{\mathsf{T}}\boldsymbol{f}_{\mathrm{IB}} = \boldsymbol{u}_{\mathrm{B}}^{\mathsf{T}}\boldsymbol{f}_{\mathrm{B}}, \tag{36}$$

where $\boldsymbol{f}_{\mathrm{IB}}$ is the interface force vector equivalent to the BEM forces. Substituting Eq. (27) one can write

$$\boldsymbol{f}_{\mathrm{IB}} = \boldsymbol{f}_{\mathrm{B}}. \tag{37}$$

On the other hand, one can derive the equivalence between the DEM and the interface as

$$\boldsymbol{u}_{\mathrm{I}}^{\mathsf{T}}\boldsymbol{f}_{\mathrm{ID}} = \boldsymbol{u}_{\mathrm{D}}^{\mathsf{T}}\boldsymbol{f}_{\mathrm{D}}, \tag{38}$$

where $\boldsymbol{f}_{\mathrm{ID}}$ is the interface force vector equivalent to the DEM forces. Substituting Eq. (33) one can write

$$\boldsymbol{u}_{\mathrm{I}}^{\mathsf{T}}\boldsymbol{f}_{\mathrm{ID}} = \boldsymbol{u}_{\mathrm{I}}^{\mathsf{T}}\boldsymbol{T}^{\mathsf{T}}\boldsymbol{f}_{\mathrm{D}}, \tag{39}$$

and, hence,

$$\boldsymbol{f}_{\mathrm{ID}} = \boldsymbol{T}^{\mathsf{T}}\boldsymbol{f}_{\mathrm{D}}. \tag{40}$$

4. Time integration

4.1. Monolithic time integration

In the monolithic time integration scheme, both methods progress in time simultaneously. Hence, $i = j$ and $\Delta t_{\mathrm{D}}^{(i)} = \Delta t_{\mathrm{B}} \forall i$. Therefore, the compatibility and equilibrium equations at the interface must be imposed directly. Consequently, it is necessary to assemble and solve a unified set of equations. To do that, both methods must be adapted as proposed by Barros et al. [59].

In the DEM, the Central Difference (CD) derivative approximation is used to transform accelerations directly into displacements and angular accelerations in rotations, such as

$$\ddot{\boldsymbol{u}}_{\mathrm{D}}^{(i)} = \frac{\boldsymbol{u}_{\mathrm{D}}^{(i+1)} - 2\boldsymbol{u}_{\mathrm{D}}^{(i)} + \boldsymbol{u}_{\mathrm{D}}^{(i-1)}}{\Delta t_{\mathrm{D}}^2}, \tag{41}$$

which allows one to write a dynamic stiffness-like equilibrium equation, which was derived in [59]:

$$\boldsymbol{f}_{\mathrm{D}}^{(i+1)} = \boldsymbol{K}_{\mathrm{D}}\boldsymbol{u}_{\mathrm{D}}^{(i+1)} - \boldsymbol{h}_{\mathrm{D}}^{(i+1)}. \tag{42}$$

The difference between Eq. (42) and the similar one present in the work of Barros et al. [59] is that the displacement vector here also contains rotations. Hence, $\boldsymbol{f}_{\mathrm{D}}^{(i+1)}$ contains moments and forces, and $\boldsymbol{K}_{\mathrm{D}}$ depends not only on the mass but also on the particle's rotational inertia.

In the BEM, one needs to isolate the traction at $i+1$ and then transform it into equivalent nodal forces to find

$$\boldsymbol{f}_{\mathrm{B}}^{(i+1)} = \boldsymbol{K}_{\mathrm{B}}\boldsymbol{u}_{\mathrm{B}}^{(i+1)} - \boldsymbol{h}_{\mathrm{B}}^{(i+1)}. \tag{43}$$

Note that Eq. (43) is exactly equal to the corresponding one in Ref. [59].

The substitution of Eqs. (33) and (40) into Eq. (42) gives

$$\boldsymbol{f}_{\mathrm{ID}}^{(i+1)} + \boldsymbol{T}^{\mathsf{T}} \boldsymbol{f}_{\mathrm{D}}^{(i+1)} = \boldsymbol{T}^{\mathsf{T}} \boldsymbol{K}_{\mathrm{D}} \boldsymbol{T} \boldsymbol{u}_{\mathrm{I}}^{(i+1)} - \boldsymbol{T}^{\mathsf{T}} \boldsymbol{h}_{\mathrm{D}}^{(i+1)} , \tag{44}$$

where the term $\boldsymbol{f}_{\mathrm{ID}}^{(i+1)}$ is added to consider the forces applied by the interface onto the particles. In addition, substituting Eqs. (27) and (37) into Eq. (43) gives

$$\boldsymbol{f}_{\mathrm{IB}}^{(i+1)} + \boldsymbol{f}_{\mathrm{B}}^{(i+1)} = \boldsymbol{K}_{\mathrm{B}} \boldsymbol{u}_{\mathrm{I}}^{(i+1)} - \boldsymbol{h}_{\mathrm{B}}^{(i+1)} , \tag{45}$$

where $\boldsymbol{f}_{\mathrm{IB}}^{(i+1)}$ represents the forces from the interface onto the BEM. The equilibrium condition must be satisfied at the interface, hence,

$$\boldsymbol{f}_{\mathrm{ID}}^{(i+1)} + \boldsymbol{f}_{\mathrm{IB}}^{(i+1)} = \boldsymbol{0} . \tag{46}$$

Eqs. (44) and (45) are combined into

$$\boldsymbol{f}_{\mathrm{I}}^{(i+1)} = \boldsymbol{K}_{\mathrm{I}} \boldsymbol{u}_{\mathrm{I}}^{(i+1)} - \boldsymbol{h}_{\mathrm{I}}^{(i+1)} , \tag{47}$$

with

$$\boldsymbol{f}_{\mathrm{I}}^{(i+1)} = \boldsymbol{f}_{\mathrm{B}}^{(i+1)} + \boldsymbol{T}^{\mathsf{T}} \boldsymbol{f}_{\mathrm{D}}^{(i+1)} , \tag{48}$$

$$\boldsymbol{h}_{\mathrm{I}}^{(i+1)} = \boldsymbol{h}_{\mathrm{B}}^{(i+1)} + \boldsymbol{T}^{\mathsf{T}} \boldsymbol{h}_{\mathrm{D}}^{(i+1)} , \tag{49}$$

and

$$\boldsymbol{K}_{\mathrm{I}} = \boldsymbol{K}_{\mathrm{B}} + \boldsymbol{T}^{\mathsf{T}} \boldsymbol{K}_{\mathrm{D}} \boldsymbol{T} . \tag{50}$$

After solving Eq. (47), Eqs. (27) and (33) give the BEM and DEM displacements, respectively.

4.2. Staggered time integration

In the conventional monolithic coupling scheme, the DEM and the BEM are solved simultaneously at each time step. The first drawback of this approach is that the matrices of each method need to be known to assemble a coupled system of equations. Therefore, the methods cannot be independently used as 'black boxes'. The second drawback is that finding a single time step size to satisfy both methods is challenging, as there is a significant disparity between the required time steps. In addition, if this time step exists, it can lead to high computational costs. To address these challenges, this section presents a staggered coupling scheme. This scheme separately solves the governing equations of the DEM and BEM at different time instants. This approach allows for a larger time step in the BEM, resulting in significant computational savings while maintaining the accuracy of the solution. In the following, it is assumed that the BEM discretises time in j time steps of constant size Δt_{B}, so that $t_{\mathrm{B}}^{(j)} = j \Delta t_{\mathrm{B}}$. Additionally, the DEM discretises time in i time steps of varying sizes, so that $t_{\mathrm{D}}^{(i)} = \sum_{k=0}^{i} \Delta t_{\mathrm{D}}^{(k)}$. Therefore, the number of time steps of the DEM and the BEM are i and j, respectively.

As discussed in Section 4.1, two conditions must be satisfied at the interface: the equilibrium of forces and the compatibility of displacements. To address these requirements, the staggered scheme distinguishes between the two conditions and assigns each method or subdomain the responsibility for one of them. Consequently, either a Neumann or Dirichlet boundary condition is applied at the interface of the subdomains. This results in two possible coupling approaches, the Dirichlet–Neumann and the Neumann–Dirichlet, depending on the condition appearing in the BEM and the DEM, respectively. The incorporation of non-conforming interfaces in the staggered coupling is analogous to the monolithic coupling.

4.2.1. Dirichlet-Neumann approach

The idea behind this staggered scheme is to first apply the interface displacements at the BEM region to compute the forces resulting from these displacements. Secondly, integrate the motion of DEM particles using these forces. Then, the updated particle displacements are applied to the BEM, restarting the process.

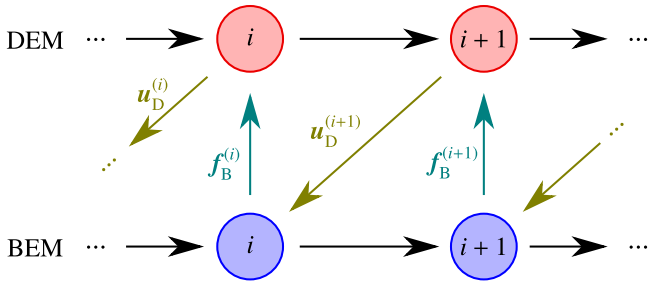

Fig. 4. Dirichlet–Neumann staggered BEM-DEM coupling where the yellow lines represent displacements and the cyan lines forces. (For interpretation of the references to colour in this figure legend, the reader is referred to the web version of this article.)

To perform the described procedure, it is necessary to solve the motion of the particles constrained to the interface admissible motion. This can be achieved first by writing Eqs. (1) and (2) in matrix form for all interface particles as

$$\boldsymbol{M}\ddot{\boldsymbol{u}}_{\mathrm{D}}^{(i)} = \boldsymbol{f}_{\mathrm{D}}^{(i)} , \tag{51}$$

where $\boldsymbol{M}$ is the inertia matrix containing the mass and inertia of particles along the diagonal, $\ddot{\boldsymbol{u}}_{\mathrm{D}}$ is the acceleration vector taken as the second time-derivative of Eq. (32), and $\boldsymbol{f}_{\mathrm{D}}$ is the collection of all forces and torques acting on this particles in vector form. Secondly, substitute Eqs. (33) and (40) into Eq. (51) to find

$$\boldsymbol{T}^{\mathsf{T}}\boldsymbol{f}_{\mathrm{D}}^{(i)} = \boldsymbol{T}^{\mathsf{T}}\boldsymbol{M}\boldsymbol{T}\ddot{\boldsymbol{u}}_{\mathrm{I}}^{(i)} . \tag{52}$$

This is an equation of motion for the nodes of the interface. Even though interface nodes do not have their own masses and no force is directly applied to them, a mass matrix is derived for these nodes as $\boldsymbol{M}_{\mathrm{I}} = \boldsymbol{T}^{\mathsf{T}}\boldsymbol{M}\boldsymbol{T}$. This mass matrix is made of the contribution of the mass and inertia of each particle at the interface. After solving equation Eq. (52) for the accelerations of interface nodes, the accelerations of particles at the interface are determined by Eq. (35). Finally, the interface node accelerations are then integrated in time using the "leapfrog" method (Eqs. (5)–(7)) to find the interface node displacements, which give the BEM displacement via Eq. (27).

This is the general idea of the staggered scheme. Some intricacies depend on whether the time steps are equal or different and if there exist time instants to which the methods coincide. The schematic in Fig. 4 represents the staggered coupling using the same time step for both methods. This staggered coupling is implemented in Algorithm 1.

Since the staggered scheme handles the equations of each method separately, different time steps are allowed. This is called multi-scale time integration. In the Dirichlet–Neumann approach, the BEM force is kept constant, while the DEM motion is updated for several time steps. Once the DEM has marched over the next time instant of the BEM, the BEM displacement at this instant can be determined through a linear interpolation as

$$\boldsymbol{u}_{\mathrm{B}}\left(t^{(j)}\right) = \boldsymbol{u}_{\mathrm{I}}^{(i)} + \left(\boldsymbol{u}_{\mathrm{I}}^{(i+1)} - \boldsymbol{u}_{\mathrm{I}}^{(i)}\right)\frac{t^{(j)} - t^{(i)}}{t^{(i+1)} - t^{(i)}} = \boldsymbol{u}_{\mathrm{I}}^{(i)} + \dot{\boldsymbol{u}}_{\mathrm{I}}^{\left(i+\frac{1}{2}\right)}\left(t^{(j)} - t^{(i)}\right) , \tag{53}$$

which is equivalent to using the same corresponding "leapfrog" velocity, only with a different time increment. This approach is schematically illustrated in Fig. 5. Algorithm 2 shows the implementation of the coupling using the staggered multi-scale time integration.

4.2.2. Neumann-Dirichlet approach

Alternatively, a staggered scheme can be crafted by applying the DEM forces to the interface and taking the interface displacement equal to the BEM displacement. In this approach, the BEM has Neumann boundary conditions at the interface, while the DEM has Dirichlet boundary conditions. Fig. 6 schematically represents the Neumann–Dirichlet staggered coupling and Algorithm 3 describes its implementation.

A similar approach to the one on Section 4.2.1 can be used here to enable different time steps in each method and to allow the DEM time step to vary, as schematically illustrated in Fig. 7. However, the fact that the DEM

Algorithm 1: Dirichlet–Neumann staggered time integration for non-conforming coupling

Based on the interface particle initial positions and the elements on the interface, compute the compatibility matrix $\boldsymbol{T}$;
Assemble the mass matrix $\boldsymbol{M}$ summing up the contribution of the mass and inertia of each particle at the interface;
Compute $\boldsymbol{T}^{\mathsf{T}}\boldsymbol{M}\boldsymbol{T}$ and store its Cholesky factorisation;
for $i = 0$ **to** N **do**
  Compute BEM forces $\boldsymbol{f}_{\mathrm{B}}^{(i)}$ as in Eq. (43);
  Compute contact forces and moments at DEM particles $\boldsymbol{f}_p^{(i)}$ and $\mathcal{M}_p^{(i)}$ as per Eqs. (3) and (4);
  Assemble the force vector for interface particles $\boldsymbol{f}_{\mathrm{D}}^{(i)}$;
  Calculate total force at interface $\boldsymbol{f}_{\mathrm{I}}^{(i)}$;
  Solve Eq. (52) for the accelerations of the interface $\ddot{\boldsymbol{u}}_{\mathrm{I}}^{(i)}$;
  Compute translational and rotational accelerations for interface particles via Eq. (35);
  Calculate accelerations of all other particles p as $\ddot{\boldsymbol{u}}_p^{(i)} = \frac{\boldsymbol{f}_p^{(i)}}{m_p}$;
  Integrate motion of all particles (including the ones at the interface) through Eqs. (5)–(10);
  Find the displacements of the interface nodes at the next time step $\boldsymbol{u}_{\mathrm{I}}^{(i+1)}$ using the "leapfrog" method (Eqs. (5)–(7));
  Apply the BEM displacements at the next time step $\boldsymbol{u}_{\mathrm{B}}^{(i+1)} = \boldsymbol{u}_{\mathrm{I}}^{(i+1)}$;

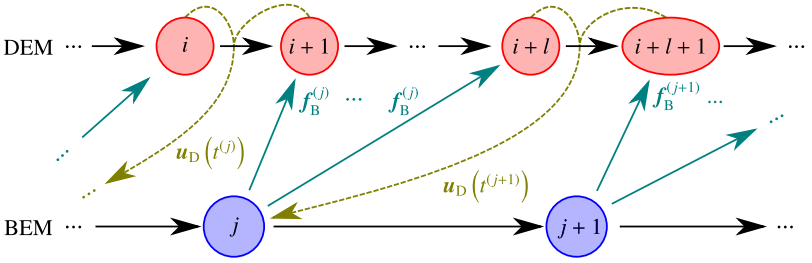

Fig. 5. Dirichlet–Neumann multi-scale time staggered BEM-DEM coupling where the yellow dashed lines represent interpolated displacements and the cyan lines forces. (For interpretation of the references to colour in this figure legend, the reader is referred to the web version of this article.)

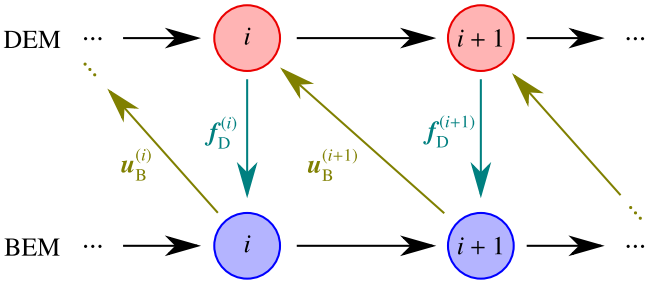

Fig. 6. Neumann–Dirichlet staggered BEM-DEM coupling where the yellow lines represent displacements and the cyan lines forces. (For interpretation of the references to colour in this figure legend, the reader is referred to the web version of this article.)

force varies within each BEM time-step poses an additional challenge. The solution proposed here is based on the work by Cornejo et al. [65]. It consists of calculating the impulse $\boldsymbol{I}$ created by the DEM force in all sub-steps as

$$\boldsymbol{I}_{\mathrm{I}}^{(i+1)} = \boldsymbol{I}_{\mathrm{I}}^{(i)} + \boldsymbol{T}^{\mathsf{T}} \boldsymbol{f}_{\mathrm{D}}^{(i)} \Delta t_{\mathrm{D}}^{(i)} \,. \tag{54}$$

Algorithm 2: Dirichlet–Neumann staggered multi-scale time integration for non-conforming coupling

Based on the interface particle initial positions and the elements on the interface, compute the compatibility matrix $\boldsymbol{T}$;
Assemble the mass matrix $\boldsymbol{M}$ summing up the contribution of the mass and inertia of each particle at the interface;
Compute $\boldsymbol{T}^{\mathsf{T}}\boldsymbol{M}\boldsymbol{T}$ and store its Cholesky factorisation;
$j \leftarrow 0$;
for $i = 0$ **to** N **do**
  Compute BEM forces $\boldsymbol{f}_{\mathrm{B}}^{(j)}$ as in Eq. (43);
  Compute contact forces and moments at DEM particles $\boldsymbol{f}_p^{(i)}$ and $\mathcal{M}_p^{(i)}$ as per Eqs. (3) and (4);
  Assemble the force vector for interface particles $\boldsymbol{f}_{\mathrm{D}}^{(i)}$;
  Calculate total force at interface $\boldsymbol{f}_{\mathrm{I}}^{(i)} = \boldsymbol{T}^{\mathsf{T}}\boldsymbol{f}_{\mathrm{D}}^{(i)} + \boldsymbol{f}_{\mathrm{B}}^{(j)}$;
  Solve Eq. (52) for the accelerations of the interface $\ddot{\boldsymbol{u}}_{\mathrm{I}}^{(i)}$;
  Compute translational and rotational accelerations for interface particles via Eq. (35);
  Calculate accelerations of all other particles p as $\ddot{\boldsymbol{u}}_p^{(i)} = \frac{\boldsymbol{f}_p^{(i)}}{m_p}$;
  Integrate the motion of all particles (including the ones at the interface) through Eqs. (5)–(10);
  Integrate the motion of the interface nodes using the "leapfrog" method (Eqs. (5)–(7)) to determine their displacement at the next time step $\boldsymbol{u}_{\mathrm{I}}^{(i+1)}$;
  if $t^{(i+1)} \geq t^{(j+1)}$ **then**
    Interpolate the interface displacements at $j+1$ through Eq. (53);
    Apply the BEM displacements at the next time step $\boldsymbol{u}_{\mathrm{B}}^{(i+1)} = \boldsymbol{u}_{\mathrm{I}}^{(i+1)}$;
    $j \leftarrow j+1$;

Algorithm 3: Neumann–Dirichlet staggered time integration for non-conforming coupling

Based on the interface particle initial positions and the elements on the interface, compute the compatibility matrix $\boldsymbol{T}$;
Store LU factorisation of the BEM stiffness matrix $\boldsymbol{K}_{\mathrm{B}}$;
for $i = 0$ **to** N **do**
  Compute contact forces and moments at DEM particles $\boldsymbol{f}_p^{(i)}$ and $\mathcal{M}_p^{(i)}$ as per Eqs. (3) and (4);
  Calculate DEM forces at the interface $\boldsymbol{f}_{\mathrm{I}}^{(i)} = \boldsymbol{T}^{\mathsf{T}}\boldsymbol{f}_{\mathrm{D}}^{(i)}$;
  Calculate total force at interface $\boldsymbol{f}_{\mathrm{I}}^{(i)}$ and apply to the BEM;
  Solve for BEM displacements taking into account external, history and interface forces $\boldsymbol{K}_{\mathrm{B}}\boldsymbol{u}_{\mathrm{B}}^{(i+1)} = \boldsymbol{f}_{\mathrm{B}}^{(i+1)} + \boldsymbol{h}_{\mathrm{B}}^{(i+1)} + \boldsymbol{T}^{\mathsf{T}}\boldsymbol{f}_{\mathrm{D}}^{(i)}$;
  Impose interface motion to DEM particles at the interface $\boldsymbol{u}_{\mathrm{D}}^{(i+1)} = \boldsymbol{T}\boldsymbol{u}_{\mathrm{I}}^{(i+1)}$;
  Calculate accelerations of all other particles p as $\ddot{\boldsymbol{u}}_p^{(i)} = \frac{\boldsymbol{f}_p^{(i)}}{m_p}$;
  Integrate motion of all particles (including the ones at the interface) through Eqs. (5)–(10);

If $t^{(i+1)} < t^{(j+1)}$, the next BEM state is farther in time then the next DEM state. It is then possible to extrapolate the force, assuming it will be constant until the next BEM state. This would create an additional impulse

$$\boldsymbol{I}_{\mathrm{I}}^{(j+1)} = \boldsymbol{I}_{\mathrm{I}}^{(i+1)} + \boldsymbol{T}^{\mathsf{T}}\boldsymbol{f}_{\mathrm{D}}^{(i)}\left(t^{(j+1)} - t^{(i+1)}\right), \tag{55}$$

which would allow calculating the force at the next BEM state as

$$\boldsymbol{f}_{\mathrm{B}}^{(j+1)} = \boldsymbol{f}_{\mathrm{I}}^{(j+1)} = \frac{\boldsymbol{I}_{\mathrm{I}}^{(j+1)}}{\Delta t_{\mathrm{B}}}. \tag{56}$$

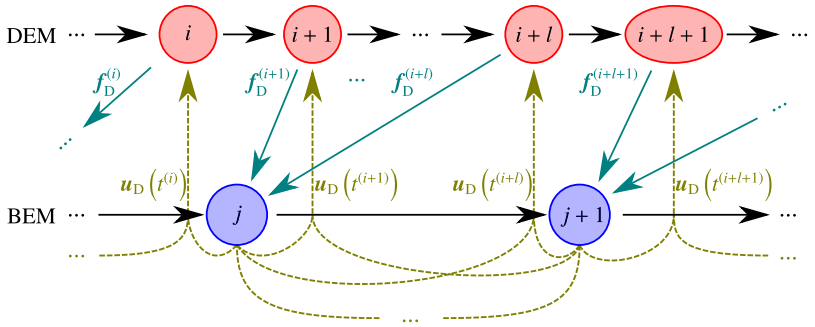

Fig. 7. Neumann–Dirichlet multi-scale time staggered BEM-DEM coupling where the yellow dashed lines represent interpolated displacements and the cyan lines forces. (For interpretation of the references to colour in this figure legend, the reader is referred to the web version of this article.)

This force is then used to estimate the displacement on the next time step of the BEM, which allows interpolating the displacements at the next step of the DEM as

$$\boldsymbol{u}_{\mathrm{I}}\left(t^{(i+1)}\right) = \boldsymbol{u}_{\mathrm{B}}^{(j)} + \left(\boldsymbol{u}_{\mathrm{B}}^{(j+1)} - \boldsymbol{u}_{\mathrm{B}}^{(j)}\right) \frac{t^{(i+1)} - t^{(j)}}{t^{(j+1)} - t^{(j)}} \,. \tag{57}$$

Algorithm 4 summarises the steps of the Neumann–Dirichlet multi-scale time coupling.

Algorithm 4: Neumann–Dirichlet staggered time integration for non-conforming coupling

Based on the interface particle initial positions and the elements on the interface, compute the compatibility matrix $\boldsymbol{T}$;
Store LU factorisation of the BEM stiffness matrix $\boldsymbol{K}_{\mathrm{B}}$;
$j \leftarrow 0$;
for $i = 0$ **to** N **do**
  Compute contact forces and moments at DEM particles $\boldsymbol{f}_p^{(i)}$ and $\mathcal{M}_p^{(i)}$ as per Eqs. (3) and (4);
  Accumulate interface impulse with DEM forces as $\boldsymbol{I}_{\mathrm{I}}^{(i+1)} = \boldsymbol{I}_{\mathrm{I}}^{(i)} + \boldsymbol{T}^{\mathsf{T}} \boldsymbol{f}_{\mathrm{D}}^{(i)} \Delta t_{\mathrm{D}}^{(i)}$;
  Calculate interface forces as $\boldsymbol{f}_{\mathrm{I}}^{(j+1)} = \frac{\boldsymbol{I}_{\mathrm{I}}^{(i+1)} + \boldsymbol{T}^{\mathsf{T}} \boldsymbol{f}_{\mathrm{D}}^{(i)} \left(t^{(j+1)} - t^{(i+1)}\right)}{\Delta t_{\mathrm{B}}}$;
  Solve for interface displacements taking $\boldsymbol{K}_{\mathrm{B}} \boldsymbol{u}_{\mathrm{I}}^{(j+1)} = \boldsymbol{f}_{\mathrm{B}}^{(j+1)} + \boldsymbol{h}_{\mathrm{B}}^{(j+1)} + \boldsymbol{f}_{\mathrm{I}}^{(j+1)}$;
  Determine interface velocity as $\dot{\boldsymbol{u}}_{\mathrm{I}}^{\left(i+\frac{1}{2}\right)} = \frac{\boldsymbol{u}_{\mathrm{I}}^{(j+1)} - \boldsymbol{u}_{\mathrm{I}}^{(j)}}{\Delta t_{\mathrm{B}}}$;
  Impose interface motion to DEM particles at the interface through Eq. (57) and $\boldsymbol{u}_{\mathrm{D}}^{(i+1)} = \boldsymbol{T} \boldsymbol{u}_{\mathrm{I}}^{(i+1)}$;
  Calculate accelerations of all other particles p as $\ddot{\boldsymbol{u}}_p^{(i)} = \frac{\boldsymbol{f}_p^{(i)}}{m_p}$;
  Integrate motion of all particles (including the ones at the interface) through Eqs. (5)–(10);
  if $t^{(i+1)} \geq t^{(j+1)}$ **then**
    Store last calculated interface displacement in the BEM $\boldsymbol{u}_{\mathrm{B}}^{(j+1)} = \boldsymbol{u}_{\mathrm{I}}^{(j+1)}$;
    $j \leftarrow j + 1$;

5. Results

5.1. Finite rod under Heaviside load

Analysing the pressure wave propagation induced by a Heaviside load in a finite rod is a classical benchmark as it has an analytical solution. The rod shown in Fig. 8(a) has length $L = 2\,\mathrm{m}$, cross-section area $A = 0.25\,\mathrm{m}^2$ and the material has Young's modulus $E = 210\,\mathrm{MPa}$ and mass density of $\rho = 7.85\,\mathrm{t/m}^3$. The Heaviside load has a magnitude over time given by $P(t) = P_0 H(t)$, where $P_0 = 21\,\mathrm{kN}$ and $H(t)$ is the Heaviside function, as shown in Fig. 8(b). While the analytical solution is formulated in one dimension, the two-dimensional modelling of this

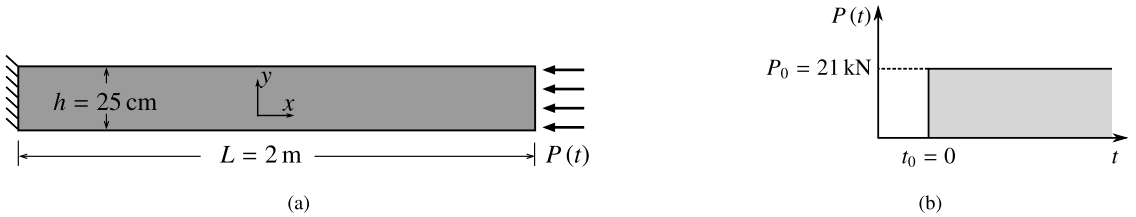

Fig. 8. Homogeneous rod under Heaviside compression load: (a) conceptual model and (b) distribution of load over time.

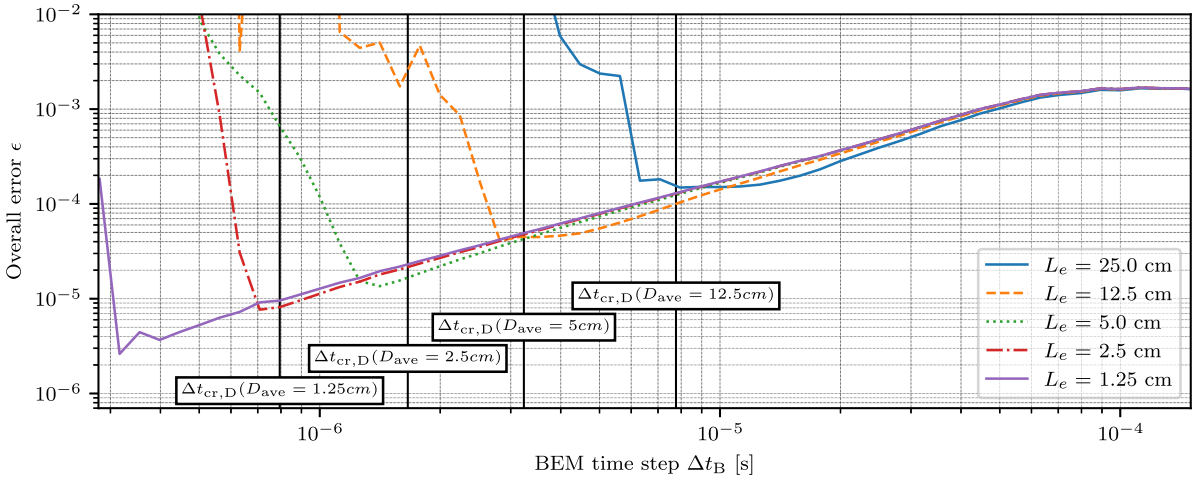

Fig. 9. Overall error of numerical models.

problem requires additional parameters. The thickness w is assumed unitary, so a height of $h = 25\,\text{cm}$ renders the desired cross-section area. In addition, the Poisson's ratio is assumed zero, *i.e.* $\nu = 0$.

As the DEM and the BEM have different ranges of time-step for which the solution is numerically stable, the model is first analysed using each method individually. To compare the accuracy of each numerical model the overall error ϵ is defined as

$$\epsilon = \int_0^T \left| \frac{u - \bar{u}_{\text{dyn}}}{\bar{u}_{\text{static}}} \right| \mathrm{d}t \tag{58}$$

where the analytical solution for the static case $\bar{u}_{\text{static}}$ normalises the difference between numerical prediction u and analytical solution of the dynamic case $\bar{u}_{\text{dyn}}$. This normalised absolute difference is then integrated over the analysis time to provide an overall measure for the error made by the analysis. Fig. 9 shows the overall error ϵ encountered for different models.

For purely DEM, a micro Poisson ratio of $\tilde{\nu} = 1.0$ is used to furnish the desired macroscopic one. The microscopic Young's modulus $\tilde{E}$ is calibrated as in [59]. Since the sought result is purely elastic, the cohesive bonds are considered unbreakable, *i.e.*, $\phi_n = \phi_s = \infty$. Five irregular assemblies of particles were generated for each average particle size $D_{\text{ave}} \in \{12.5\,\text{cm}, 5\,\text{cm}, 2.5\,\text{cm}, 1.25\,\text{cm}\}$. A uniform particle size distribution with $D \in [0.75 D_{\text{ave}}, 1.25 D_{\text{ave}}]$ is assumed. The calibrated microscopic mass density, Young's modulus, and Poisson's ratio are the same as in [59]. The analyses showed that any time step smaller than the critical one renders results with the same level of relative error. Fig. 9 shows the critical time step observed for the DEM. The overall errors ϵ are in the order of 1×10^{-2}, decreasing with the average particle size. On the other hand, the overall error ϵ of the BEM showed dependence on the geometric and time discretisation. Fig. 9 reveals that smaller time steps furnish smaller errors granted that the time step is greater than the lower stability bound. The element length L_e is the same for all boundary elements in the discretisation.

Fig. 9 evidences the inefficiency behind the conforming-monolithic coupling. For instance, the particle assembly with $D_{\text{ave}} = 1.25\,\text{cm}$ requires an element length of $L_e = 1.25\,\text{cm}$ for the particles centres to coincide with the

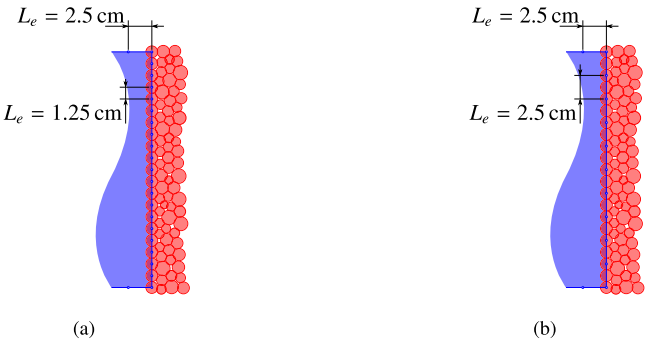

Fig. 10. Discretisation near the interface for a particle assembly with $D_{\text{ave}} = 1.25\,\text{cm}$ using: (a) conforming interface coupling, $L_e = 1.25\,\text{cm}$ at the interface and $L_e = 2.5\,\text{cm}$ elsewhere; and (b) non-conforming interface coupling, $L_e = 2.5\,\text{cm}$ everywhere.

BEM nodes. However, an element length of $L_e = 2.55\,\text{cm}$ could have been used to allow a viable time step for both methods. This is a clear indication of the inefficiency of the conforming coupling approach. The following section studies the effect of changing from conforming to non-conforming coupling. In the following analyses, the rotations are fixed as in [59].

5.1.1. Conforming vs. non-conforming interfaces

The accuracy of the proposed non-conforming coupling is put to proof using assemblies with the average particle size of $D_{\text{ave}} = 1.25\,\text{cm}$. According to Fig. 9, the critical time step of the DEM requires an element length of $L_e = 2.5\,\text{cm}$. This element length is used across the whole boundary except the interface. At the interface, the element length L_e varies from $L_e = 1.25\,\text{cm}$, which is necessary for conforming coupling (Fig. 10(a)), to the value $L_e = 2.5\,\text{cm}$ used elsewhere (Fig. 10(b)). Hence, the number of boundary elements at the interface varies from 10 to 20. All analyses used monolithic coupling with $\Delta t_{\text{D}} = \Delta t_{\text{B}} = 7.8 \times 10^{-7}\,\text{s}$.

Fig. 11 provides a comparison between the analytical result and the numerical predictions. The graph on the top shows the displacement over time, where an excellent agreement among the three curves is observed. The difference between the numerical predictions and the analytical solution normalised by the static analytical displacement is shown in the graph at the bottom, where the numerical prediction obtained with conforming and non-conforming interfaces are denoted by u_{C} and u_{NC}. It can be seen that the normalised differences between the numerical predictions and the analytical solution have the same order of magnitude and show the same behaviour over time. In fact, the difference between conforming and non-conforming, shown as a solid yellow line, needs to be multiplied by a factor of 10^2 to become visible.

Several models are analysed to further study the influence of the number of boundary elements at the interface. Fig. 12 shows the absolute difference between several numerical predictions using non-conforming interfaces and the conforming solution, which serves as a reference. The difference is normalised by the analytical displacement of the static problem. Note that the solid blue line on the bottom axes of Fig. 11 and the first column in Fig. 12 are merely different representations of the same data. By analysing Fig. 12, it can be concluded that the conforming and the non-conforming coupling approximate the analytical solution up to the same accuracy. The integral over time of these data can be carried out to provide a quantitative difference between these two models. As a matter of fact, the overall error ϵ, as defined in Eq. (58), in the conforming case is 1.17×10^{-4}, while it is 1.18×10^{-4} in the non-conforming case with ten boundary elements at the interface.

The above findings encourage the use of fewer boundary elements at the interface. However, the critical time step size of the BEM is intrinsically related to the element length. So even if, in theory, a single boundary element could be used, the time step required by the DEM of $\Delta t = 7.8 \times 10^{-7}\,\text{s}$ prohibits using a coarser discretisation. Therefore, it is imperative to use a staggered coupling scheme to improve efficiency.

5.1.2. Monolithic vs. staggered time integration

Fig. 9 shows that using an element length of $L_e = 25\,\text{cm}$ renders an overall error ϵ which is two orders of magnitude smaller than the error in the pure DEM approximation of the analytical solution. However, this

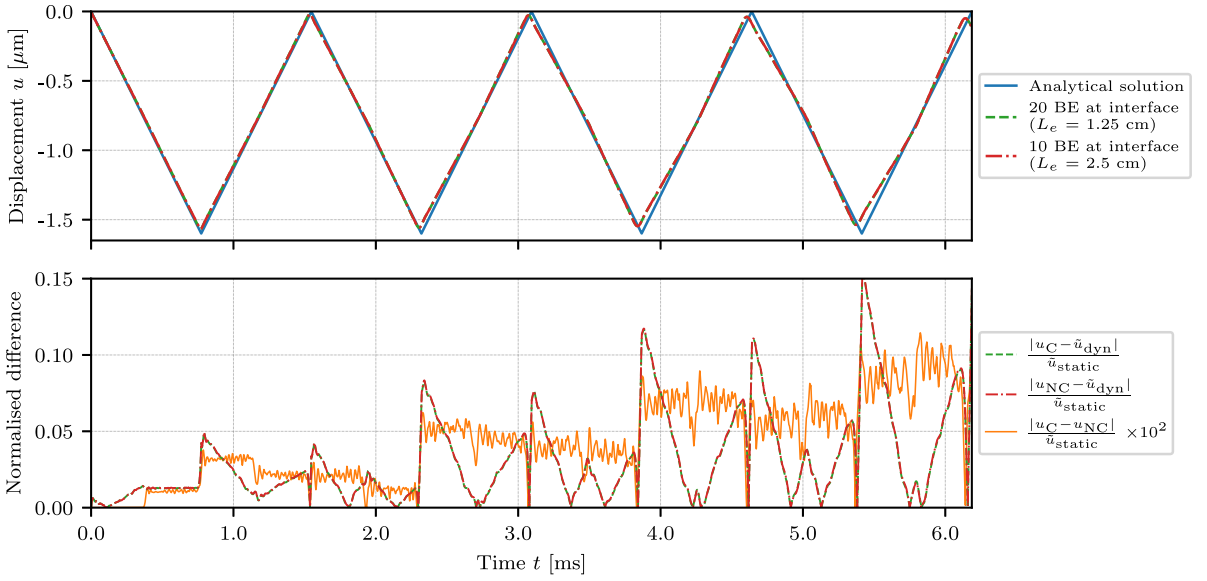

Fig. 11. Displacements from analytical and numerical solutions and relative normalised difference. The DEM assemblies have average particle size $D_{ave} = 1.25$ cm. The BEM has element length $L_e = 2.5$ cm. In the conforming coupling, the number of boundary elements at the interface is 20, which forces an element length of $L_e = 1.25$ cm at the interface.

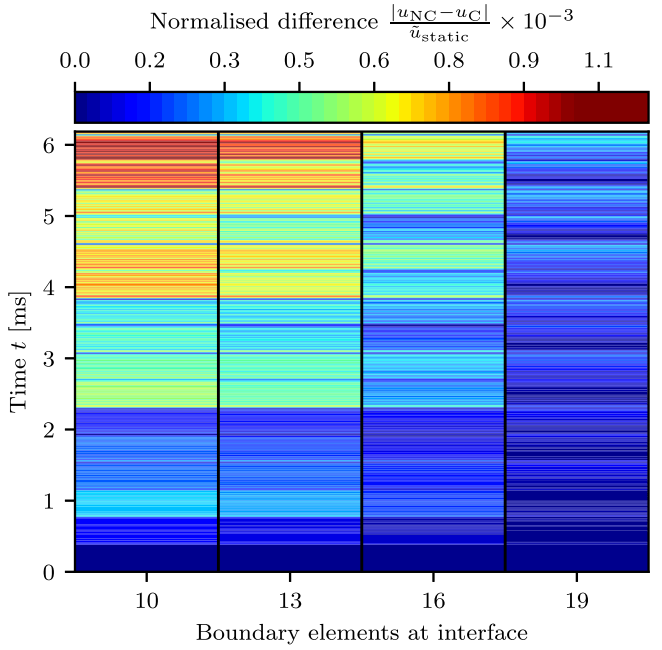

Fig. 12. Normalised difference between conforming and non-conforming coupling obtained for the assemblies with average particle size $D_{ave} = 1.25$ cm using various numbers of elements at the interface.

discretisation cannot be used in the monolithic coupling approach due to the difference in time steps required by the BEM and DEM. Specifically, while the BEM allows a minimum time-step of 8×10^{-6} s, the DEM requires a much smaller time-step of 7.8×10^{-7} s. In such a scenario, the use of a staggered scheme becomes essential to achieve a more efficient coupling.

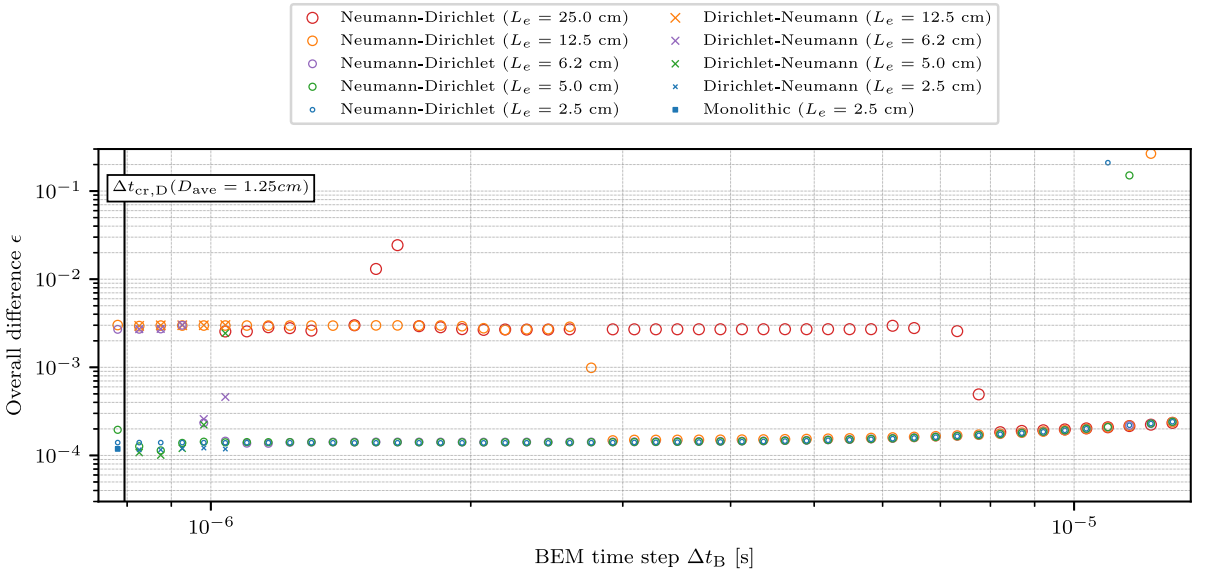

Fig. 13. Overall error ϵ comparing staggered and monolithic schemes using $\Delta t_{\mathrm{D}} = 7.8 \times 10^{-7}$ s.

Several simulations were carried out to analyse the stability and accuracy of the staggered methods presented in Section 4.2. In all simulations, the time-step of the DEM was kept fixed at 7.8×10^{-7} s. The BEM time-step varied from 7.8×10^{-7} s to 13×10^{-6} s. Five different space discretisations are considered in the BEM with element length $L_e \in \{25\,\mathrm{cm}, 12.5\,\mathrm{cm}, 6.2\,\mathrm{cm}, 5\,\mathrm{cm}, 2.5\,\mathrm{cm}\}$.

Fig. 13 shows a comparison of the overall error ϵ for each model using element lengths of $L_e = 2.5\,\mathrm{cm}$ (blue), $L_e = 5\,\mathrm{cm}$ (green), and $L_e = 25\,\mathrm{cm}$ (red). The square marker represents the monolithic solution, while the circle and cross markers correspond to Neumann–Dirichlet and Dirichlet–Neumann staggered schemes, respectively. The data indicates that the Dirichlet–Neumann is stable only if the time-step of the BEM is less than 1.1×10^{-6} s. That happens because, out of this limit, the force increment calculated in the BEM becomes too large for the DEM particles. The Neumann–Dirichlet approach proves to be much more stable.

Additionally, concerning the model with an element length of $L_e = 2.5\,\mathrm{cm}$, the Dirichlet–Neumann approach only converges to a time-step up to slightly above 1×10^{-6} s. Within this range, the time-step is too small for the spatial discretisation used in the BEM. That causes the BEM region to lock and the overall error to become much larger. At around $\Delta t_{\mathrm{B}} = 3 \times 10^{-6}$ s, convergence is observed for this element length. Only the Neumann–Dirichlet approach is convergent with this BEM time-step.

The effectiveness of the proposed methodology was evaluated by comparing it to a monolithic conforming solution. It is compared to the most computationally efficient model allowed by the proposed staggered coupling. This model utilises the Neumann–Dirichlet approach with a time step size of $\Delta t_{\mathrm{B}} = 1.3 \times 10^{-5}$ s in the BEM and an element length of $L_e = 25\,\mathrm{cm}$. This model corresponds to the right-most red circle marker in Fig. 13. The staggered solution was, on average, seven times faster and used 24 times less memory. As an example, the computation time decreased from 197 s to 30 s when running the simulations on a single core of an Intel Code i9-9980XE 3 GHz machine. The memory usage decreased from 7.2 MB to 0.3 MB.

5.2. *Cylindrical cavity in infinite space under uniform pressure*

In this problem, a long cylindrical cavity of radius $r = 1\,\mathrm{m}$ in an infinite medium (*cf.* Fig. 14(a)) is subjected to an internal pressure $p(t) = p_0 H(t)$. In other words, the pressure of magnitude $p_0 = 1.0\,\mathrm{kN/m^2}$ is applied at the beginning of the analysis and kept constant throughout, as shown in Fig. 14(b). The infinite medium has the following macroscopic material parameters: Young's modulus of $E = 100\,\mathrm{kPa}$, Poisson's ratio of $\nu = 0$, and mass density $\rho = 1.0\,\mathrm{t/m^3}$.

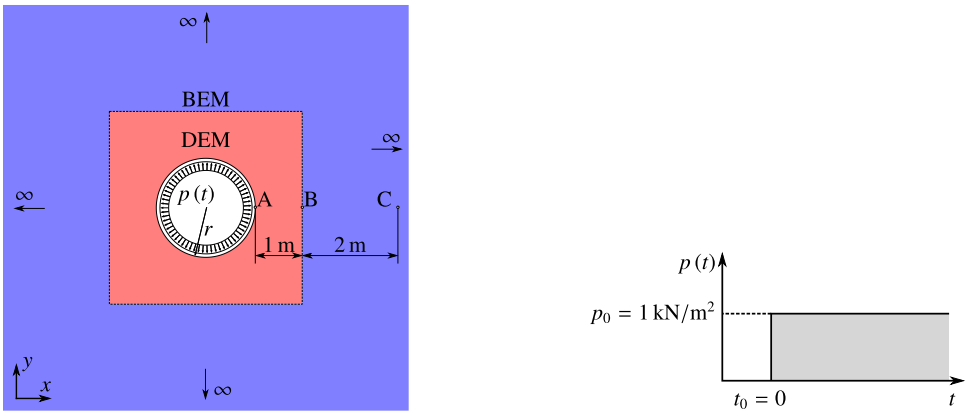

Fig. 14. Cavity in infinite medium: (a) conceptual model, (b) distribution of load over time.

The DEM is used to model the part of the domain close to the cavity, where the pressure is applied, while the BEM is used to model the remaining infinite domain. The interface between the methods consists of a square of side 4 m concentric with the cavity, as shown in Fig. 14(a). Any geometry is acceptable to the interface since it represents merely a patch in an infinite region. To make the DEM domain an annulus is reasonable because it represents the geometry of the front wave.

In the DEM modelling, a micro Poisson ratio of $\tilde{\nu} = 1.0$ is used to achieve a macroscopic one of $\nu = 0$. The micro Young's modulus was calibrated, and it was found $\tilde{E} = 27E$. Moreover, since the elastic response is considered, the cohesive bonds are unbreakable, *i.e.*, $\phi_n = \phi_s = \infty$. Three different particle assemblies were used to have an understanding of how the particle assembly affects the results. All assemblies have a uniform particle size distribution with an average particle size of $D_{\text{ave}} = 5\,\text{cm}$. The BEM region is discretised using an element length of $L_e = 25\,\text{cm}$. The time-step for the DEM is automatically determined by YADE [60] — ranging from 1×10^{-3} s to 0.9×10^{-3} s —, while for the BEM it is set to $\Delta t_{\text{B}} = 2 \times 10^{-3}$ s. For these simulations, the Neumann–Dirichlet approach is used due to its improved stability. In the following analyses, the rotations are coupled as described in Section 3.

The displacements of three points A, B and C indicated in Fig. 14(a) are used to verify the accuracy of the coupled solution. Point A: (1 m, 0) is at the cavity, Point B: (2 m, 0) is at the interface and Point C: (4 m, 0) is an internal point in the infinite BEM domain. Fig. 15 shows the displacement of points A, B, and C in blue, green and red, respectively. The solid line represents the average of the results obtained, while the maximum and minimum values are depicted in a shaded area around the average. The dashed lines are semi-analytical solutions found through numerical Laplace transforms, as proposed by Carter and Booker [66]. The dotted lines correspond to the analytical static solution to which the dynamic solution should converge after enough time is elapsed for the radiation damping to act.

Fig. 16 shows the absolute translational velocity observed in various time instants as the wave propagates from the particle assembly into the continuum. The contours of the velocities in the BEM domain are interpolated based on internal results calculated on a Delaunay triangulation [67] with a maximum triangle area of $0.05\,\text{m}^2$. In Fig. 16(b), the wave is entirely contained within the DEM region. Fig. 16(d) shows the moment the wavefront reaches the interface. In Fig. 16(e) the wavefront is partially on each domain, and it can be inferred that no significant reflection occurs. Lastly, Fig. 16(f) depicts an instant where the wavefront has completely travelled to the BEM region and will propagate towards infinity.

To measure the effectiveness of the staggered scheme, two models are compared, a monolithic and a staggered. The former used a time step of $\Delta t_{\text{D}} = \Delta t_{\text{B}} = 1 \times 10^{-3}$ s for both methods. This time step required a boundary element length of $L_e = 12.5\,\text{cm}$, which led to a non-conforming interface. In contrast, the latter used a double time step of $\Delta t_{\text{B}} = 2 \times 10^{-3}$ s in the BEM while maintaining the same time step in the DEM. As a result, the boundary element length could also be doubled to $L_e = 25\,\text{cm}$. The computational time and memory usage of the latter method showed an improvement of 4 times.

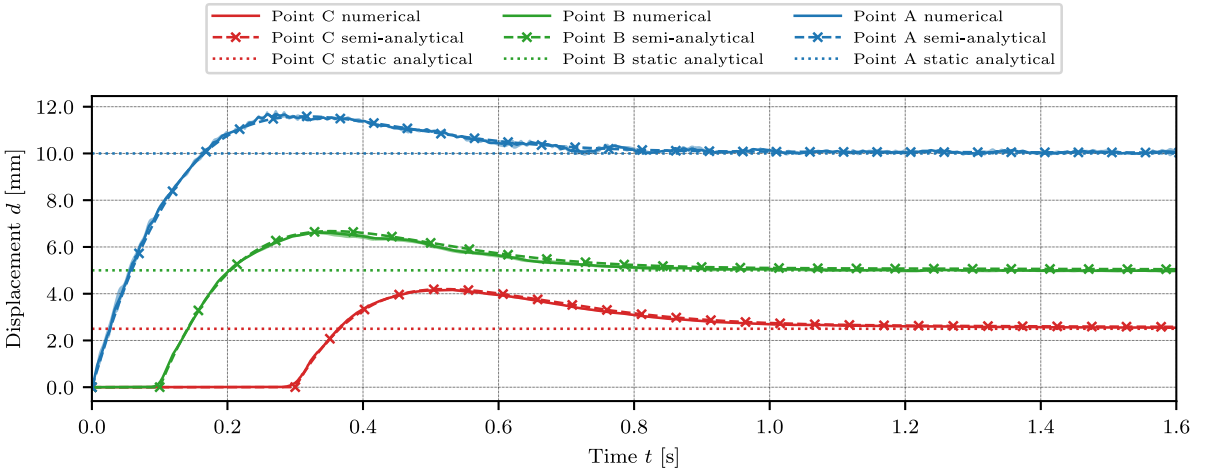

Fig. 15. Displacements over time in cavity example using the Neumann–Dirichlet staggered approach with $D_{\text{ave}} = 5\,\text{cm}$, Δt_{D} automatically defined by YADE, $L_e = 25\,\text{cm}$, and $\Delta t_{\text{B}} = 2 \times 10^{-3}\,\text{s}$.

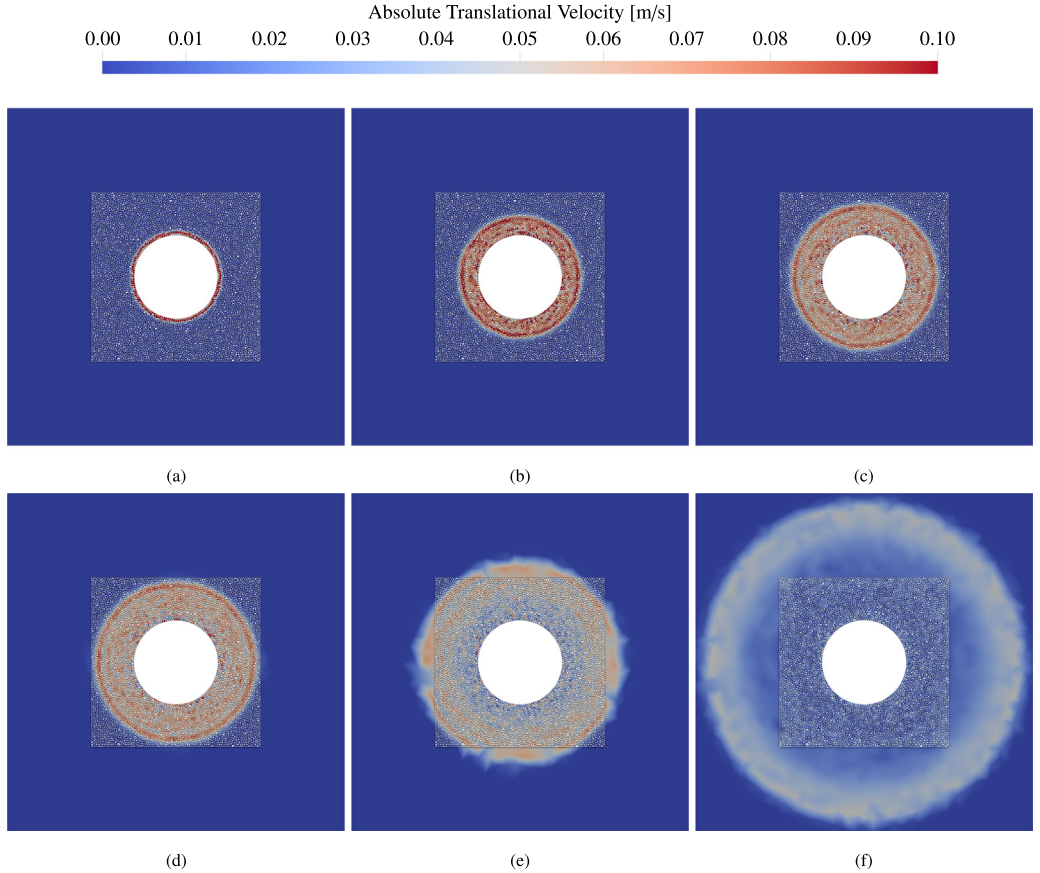

Fig. 16. Absolute translational velocity in the elastic cavity benchmark problem at: (a) 9 ms, (b) 47 ms, (c) 75 ms, (d) 93 ms, (f) 140 ms, (f) 279 ms. See Appendix online version for the video.

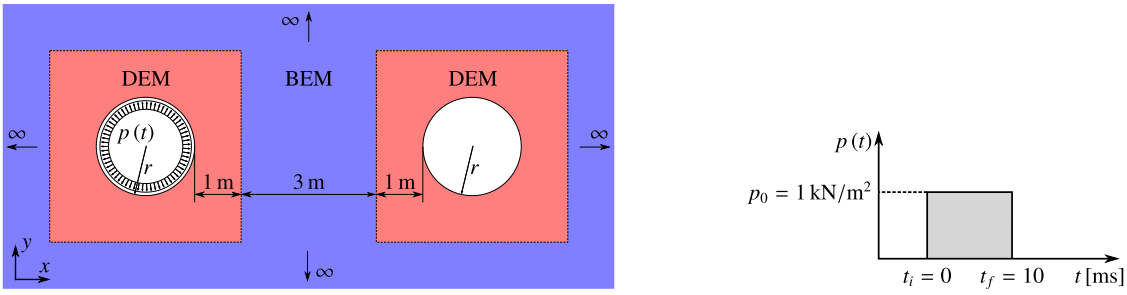

Fig. 17. Cavity in infinite medium: (a) conceptual model, (b) distribution of load over time.

5.3. Explosion in adjacent cavities

This example involves applying a blast loading in a cavity and studying how the wave propagates to an adjacent cavity, as fracturing damages the material. The cavities are 5 m apart, as shown in Fig. 17. The elastic parameters of the medium are the same as in Section 5.2. The normal cohesion is $\phi_n = 110\,\text{kN}$ and the ratio between normal and shear cohesion is $\phi_n/\phi_s = 1/3$. The internal pressure has the same load as in Section 5.2, but a limited duration of 10 ms.

Fig. 18 displays the absolute translational velocity for various time intervals. Fig. 18(b) exhibits a moment where the wave is partially in each domain without any observable reflection. Fig. 18(c) illustrates a portion of the wave moving towards infinity while some parts travel towards the right-hand side cavity. In Fig. 18(d), the wavefront enters the DEM domain around the right-hand side cavity. Lastly, Fig. 18(e) shows the impact of the wave on the right-hand side cavity.

The damage progression over time is depicted in Fig. 19. The damage is calculated for each particle as the number of broken cohesive bonds divided by the initial number of bonds, *i.e.* 0 means intact and 1 all bonds are broken. One can observe that the cracks start to form around the cavity in Fig. 19(b). At this instant, the wavefront is far from the cavity, in the vicinity of the interface, as seen in Fig. 19(b). The moment the wavefront impacts the right-hand side cavity is represented by Figs. 18(e) and 19(c), where no damage can be observed. However, in Fig. 19(d), crack initiation can be seen on the left-hand side of the right-hand side cavity. Finally, Fig. 19(f) shows the damage after the crack propagation.

5.4. Cantilever wall embedded in homogeneous halfspace

This example involves a vertical cantilever wall, as depicted in Fig. 20(a), with a horizontal Heaviside load $P(t) = P_0 H(t)$ applied on the top where $P_0 = 100\,\text{kN}$ and $H(t)$ is the Heaviside function, as shown in Fig. 20(b). The wall has a unitary thickness and is made of concrete with the following elastic parameters: Young's modulus of $E_c = 30\,\text{GPa}$; Poisson's ratio of $\nu_c = 0.2$; and density $\rho_c = 2.4\,\text{t/m}^3$. The wall is partially buried in a compact soil with the following elastic parameters: Young's modulus of $E_s = 266\,\text{MPa}$; Poisson's ratio of $\nu_s = 0.35$; and density $\rho_s = 1.8\,\text{t/m}^3$.

Since no physical non-linearity is expected, the wall is modelled with pure BEM. The soil constitutes an infinite domain. The near field has stresses introduced by the interaction with the wall, and this region is modelled with DEM while the remaining is modelled with the BEM. The DEM region extends for 3 m to each side of the wall with a depth of 3 m, as shown in Fig. 20(a). The density of the particles is calculated so that the total weight of the assembly is the same as the continuum in that region. The microscopic parameters were calibrated to represent the elastic solution of the problem obtained with pure BEM representing the entire soil domain. The calibrated elastic micro parameters are the following: $\tilde{E}_s = 6.30\,\text{GPa}$ and $\tilde{\nu}_s = 1.4$. The problem is first analysed for purely elastic behaviour, then an inelastic behaviour is incorporated in the DEM.

The time step requirements vary significantly due to differences in material properties and methods used. The time step used for the wall is 1×10^{-4} s. In the BEM part of the soil, a time step of 4×10^{-4} s was adopted. The

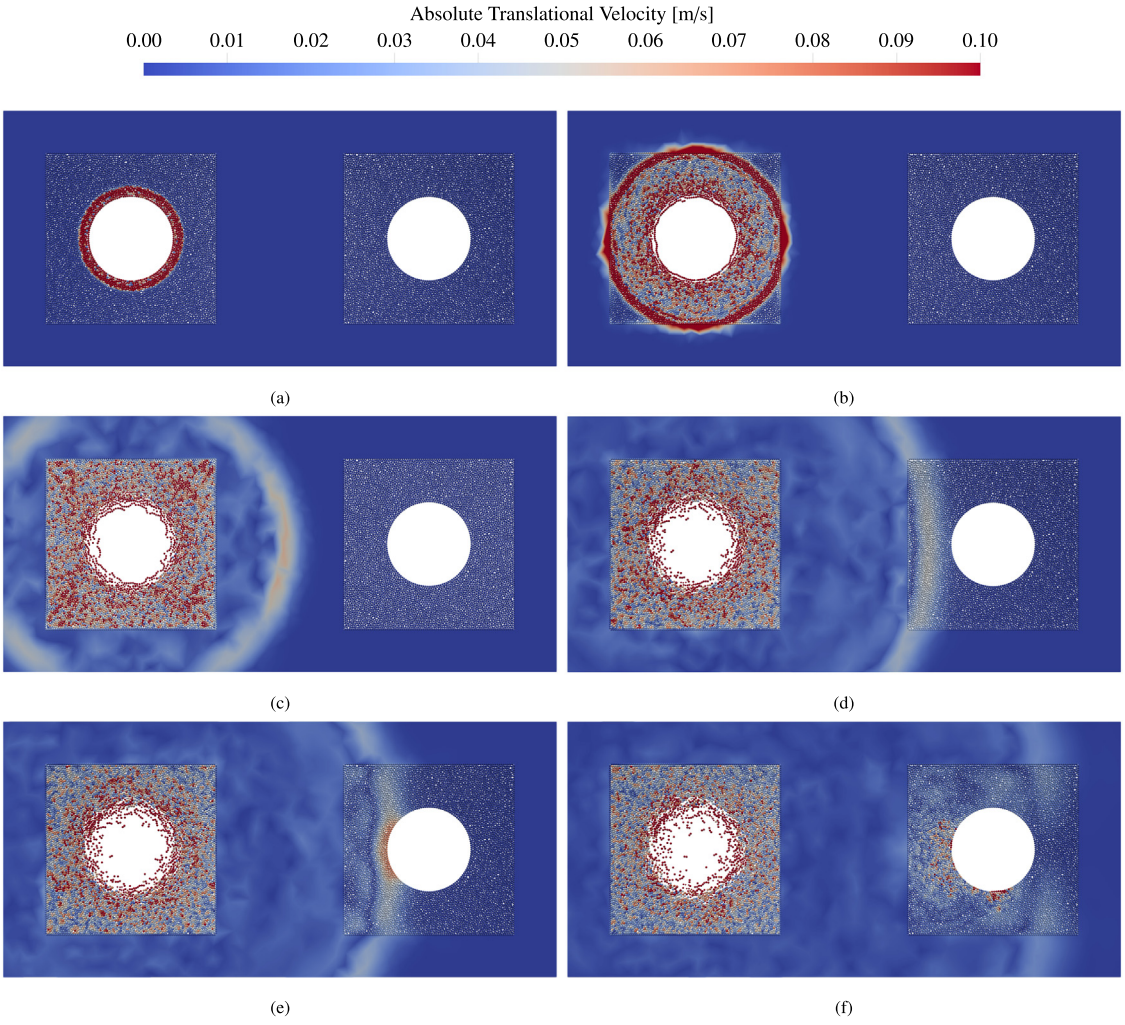

Fig. 18. Absolute translational velocity in adjacent cavities at: (a) 0.02 s, (b) 0.12 s, (c) 0.31 s, (d) 0.48 s, (e) 0.55 s. (f) 0.79 s. See Appendix online version for the video.

DEM time step size is automatically set by YADE and varies between 4.5×10^{-5} s and 5×10^{-5} s over the analysis time.

In the elastic analysis, the cohesion of the DEM interactions is infinitely large. More relevant rotations are expected in this example than in the previous examples, especially at the interface between the wall and the soil. Therefore, this is an excellent example to compare the effect of letting the rotations free as in [38], fixed as in [59], or coupled as presented in Section 3. Fig. 21 shows the predicted displacement of the top of the wall over time for the three cases of rotation considered. It can be seen that the free and fixed rotations are limiting cases to the coupled solution. The difference between them increases over time, with the fixed case deviating the most. In the case of fixed rotations, additional unrealistic contact forces are introduced, increasing the difference over time. In the case of the free rotations, the kinetic energy associated with the rotations is not transmitted to the BEM domain. Therefore, coupling the rotations allows for more realistic results.

Fig. 22 shows the velocities of particles and BEM internal nodes for various time instants. Fig. 22(a) shows the wave travelling through the wall and initiating the movements in the soil. Figs. 22(b) and 22(c) show the wave traversing the soil from the DEM to the BEM domain and travelling to infinity. In Figs. 22(d) and 22(e), it can be observed how the soil deforms as more deformation is imposed on the wall. Finally, in Fig. 22(f), an instant where

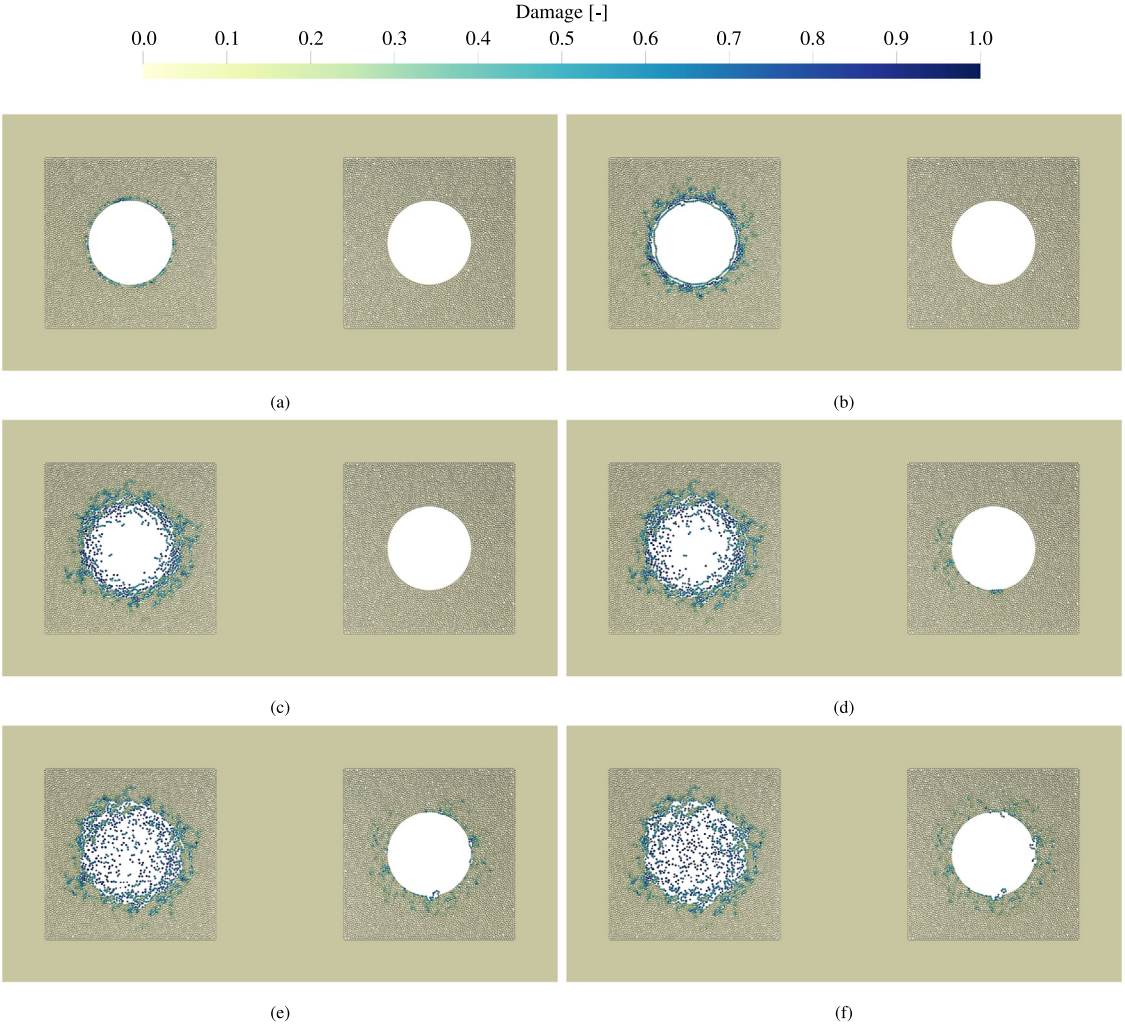

Fig. 19. Damage in adjacent cavities at: (a) 0.02 s, (b) 0.12 s, (c) 0.55 s, (d) 0.79 s, (e) 1.41 s, (f) 2.00 s. See Appendix online version for the video.

the velocities are close to zero can be seen. The elastic deformation has reached its peak, and the wall will start to move to the left towards its initial configuration.

A finite value of cohesion is assigned to the discrete material to analyse a possible failure mode in the infinite domain. The normal cohesion adopted is $\phi_n = 230\,\text{MN}$ and the ratio between normal and shear cohesion is $\phi_n/\phi_s = 1/3$. Fig. 23 shows the absolute translational velocity around crack initiation. Comparing Fig. 23 to Fig. 22, it is possible to perceive how the initiation of cracks alters the absolute translational velocity. Fig. 24 shows the damage in each particle. Figs. 24(a) and 24(b) show the crack initiating on the surface due to tensile forces exceeding the cohesive bond strength. In Figs. 24(c) and 24(d), it is possible to observe the main crack propagating downwards as a secondary one branches towards the interface. The secondary crack stops growing as the main one tilts towards the bottom of the wall creating a slipping plane failure mode as seen in Figs. 24(e) and 24(f).

6. Conclusions

This study presented a novel multi-scale time-staggered approach for coupling the DEM and the BEM. The proposed method addresses the limitations of previous BEM-DEM formulations, such as computational efficiency and numerical instability, by incorporating non-conforming interface conditions and allowing for varied time step

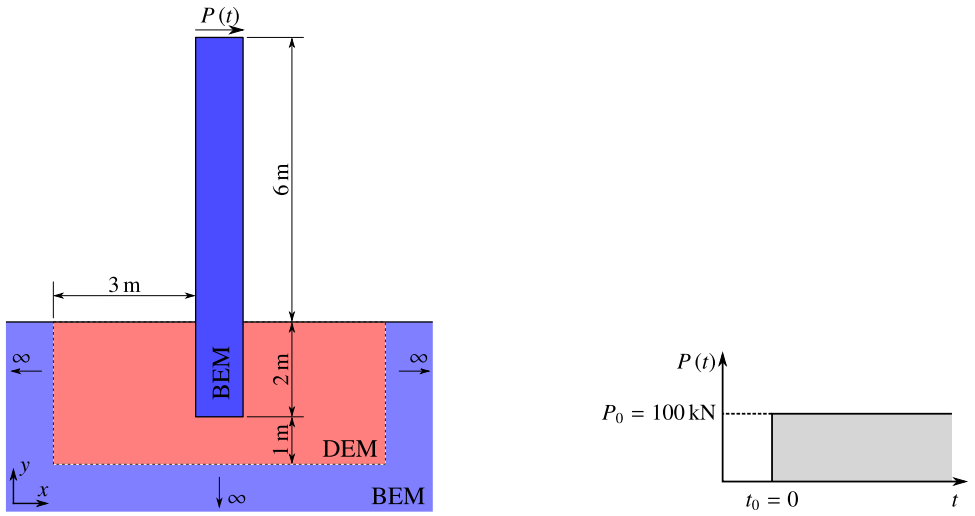

(a) (b)

Fig. 20. Cantilever wall in a halfspace: (a) conceptual model and (b) distribution of load over time.

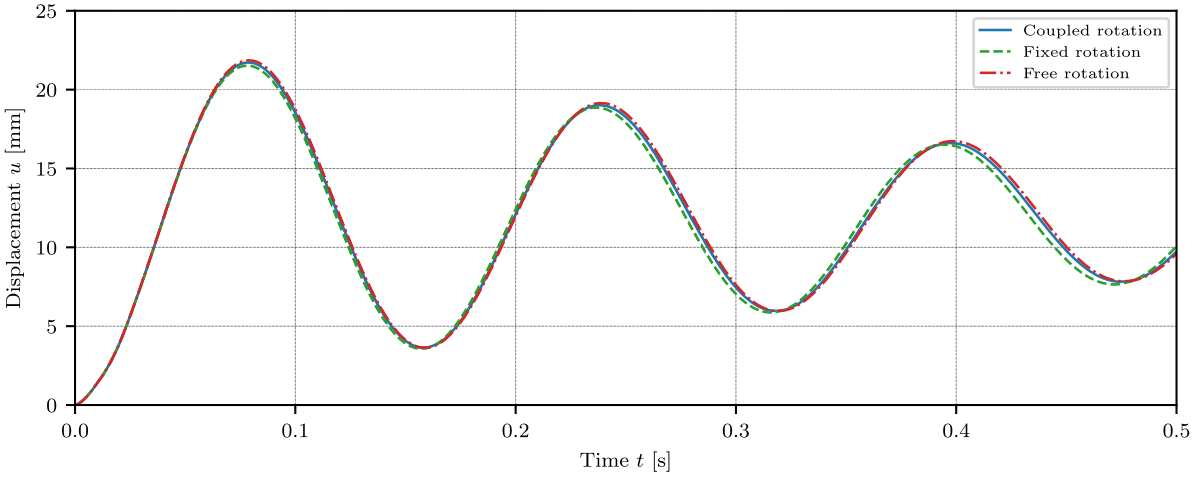

Fig. 21. Displacement of the top of the wall over time for different consideration of the rotational DOF.

sizes. Integrating the coupling of rotations further enables more realistic simulations by accounting for rotational DOFs at the interface.

The numerical examples demonstrated that the proposed method enhances accuracy and computational efficiency compared to existing methods without loss of accuracy. Two possible staggered schemes, Neumann–Dirichlet and Dirichlet–Neumann, were investigated, with the Neumann–Dirichlet scheme proving to be more stable and allowing for a broader range of time step sizes. The non-conforming interface conditions reduce the computational cost by enabling bigger BEM element lengths up to a factor of 5. The BEM time step could be increased by a factor of 20. Overall, the staggered scheme decreased computational time by up to 7 times and reduced memory consumption by a factor of 24. While the primary focus of this paper is on enhancing the coupling scheme, there is certainly room for improvement in the computational efficiency of each method. The BEM, for instance, can benefit from compression schemes to improve both its computational efficiency and memory usage.

The outlined improvements contribute to a more robust and efficient BEM-DEM coupling, facilitating its application in various engineering problems. Future research will focus on extending the proposed approach to three-dimensional problems and incorporating additional material models for more complex simulations, including

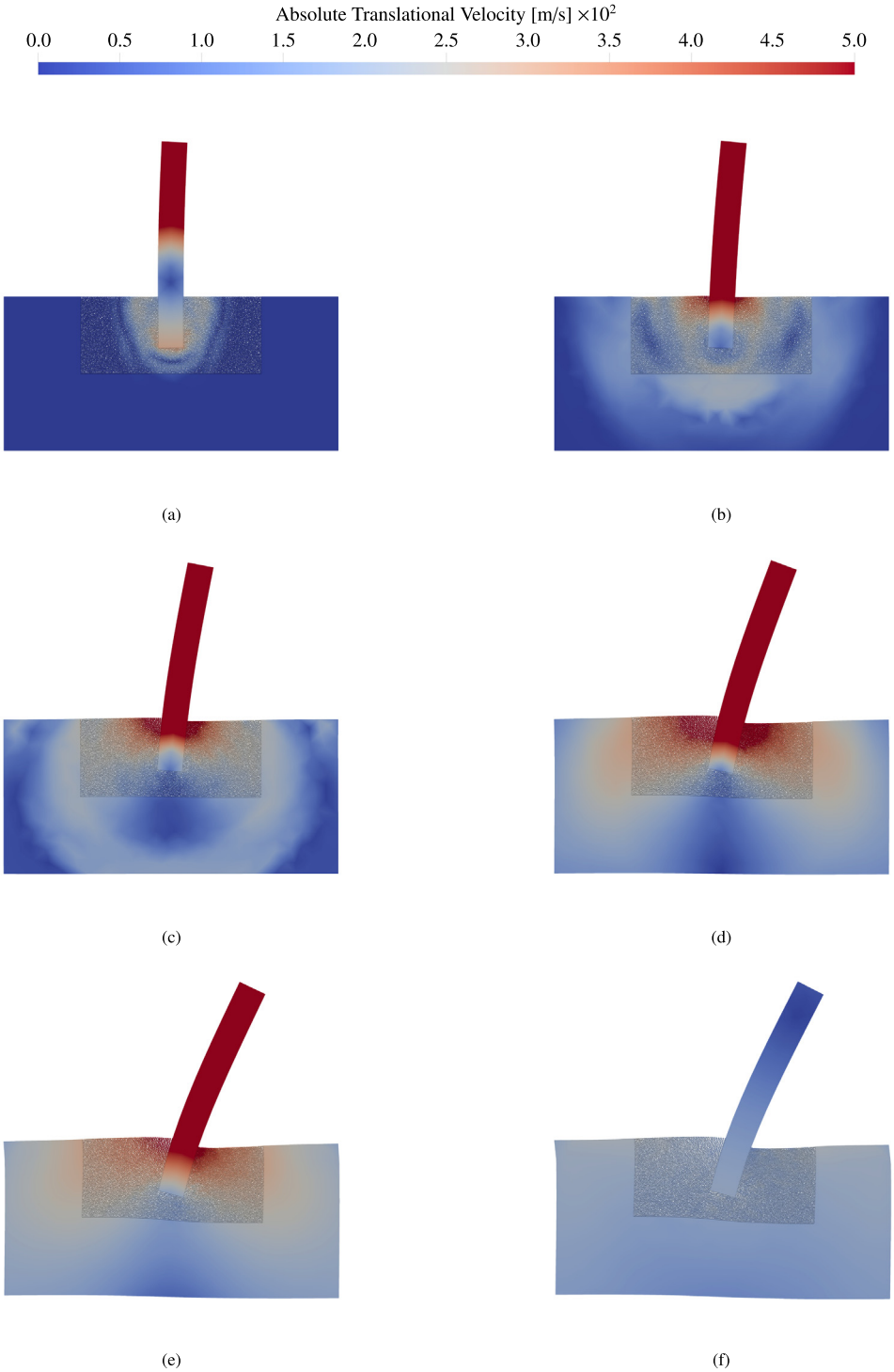

Fig. 22. Velocity of wall and surrounding soil at: (a) 9.6 ms, (b) 19.1 ms, (c) 31.9 ms, (d) 51 ms, (e) 67 ms, (f) 82.9 ms. Displacements are exaggerated by a factor of 150. See Appendix online version for the video.

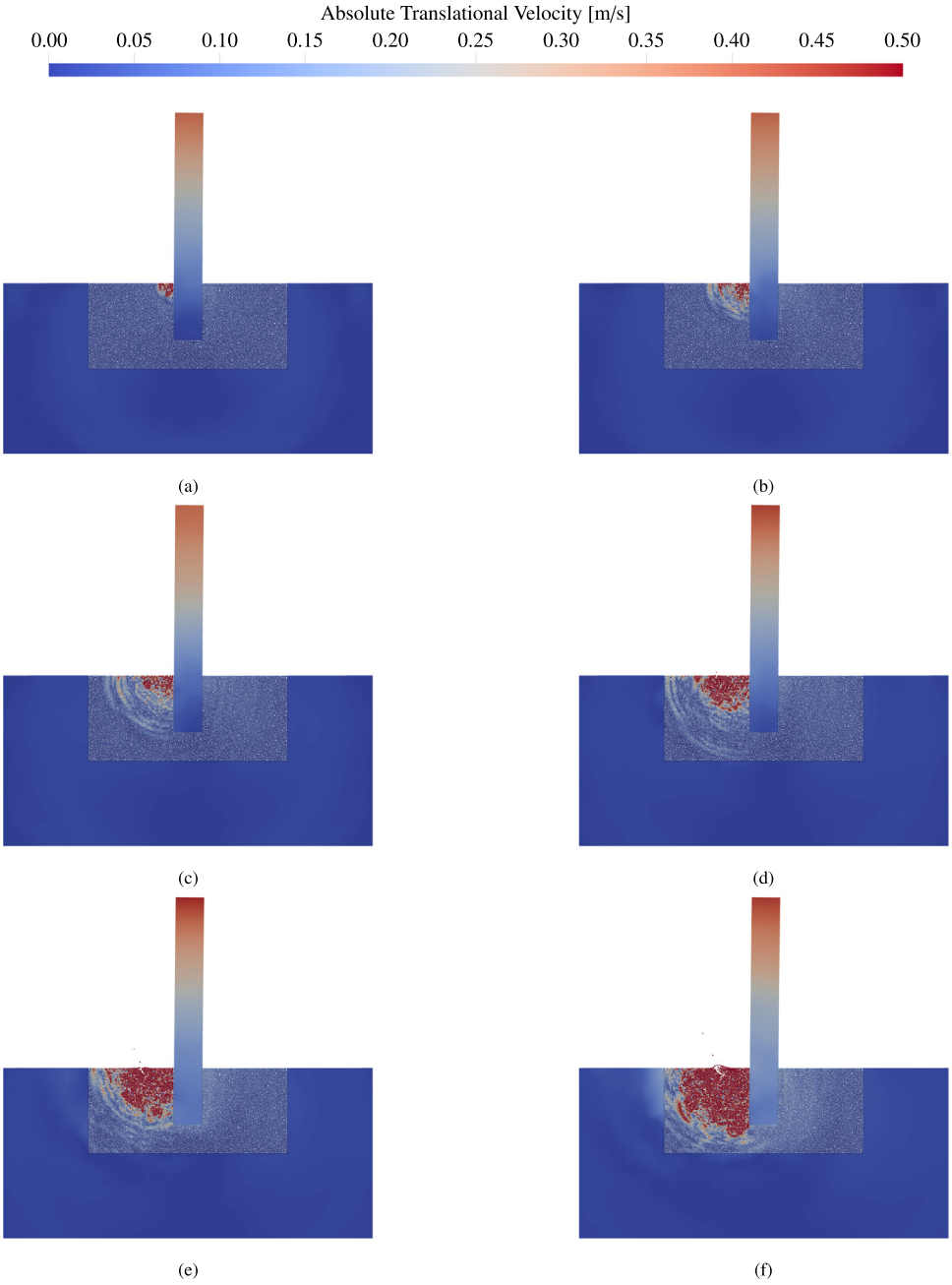

Fig. 23. Velocity profile close to crack initiation: (a) 30 ms, (b) 32 ms, (c) 35 ms, (d) 37 ms, (e) 40 ms, (f) 42 ms. Displacements are exaggerated by a factor of 5. See Appendix online version for the video.

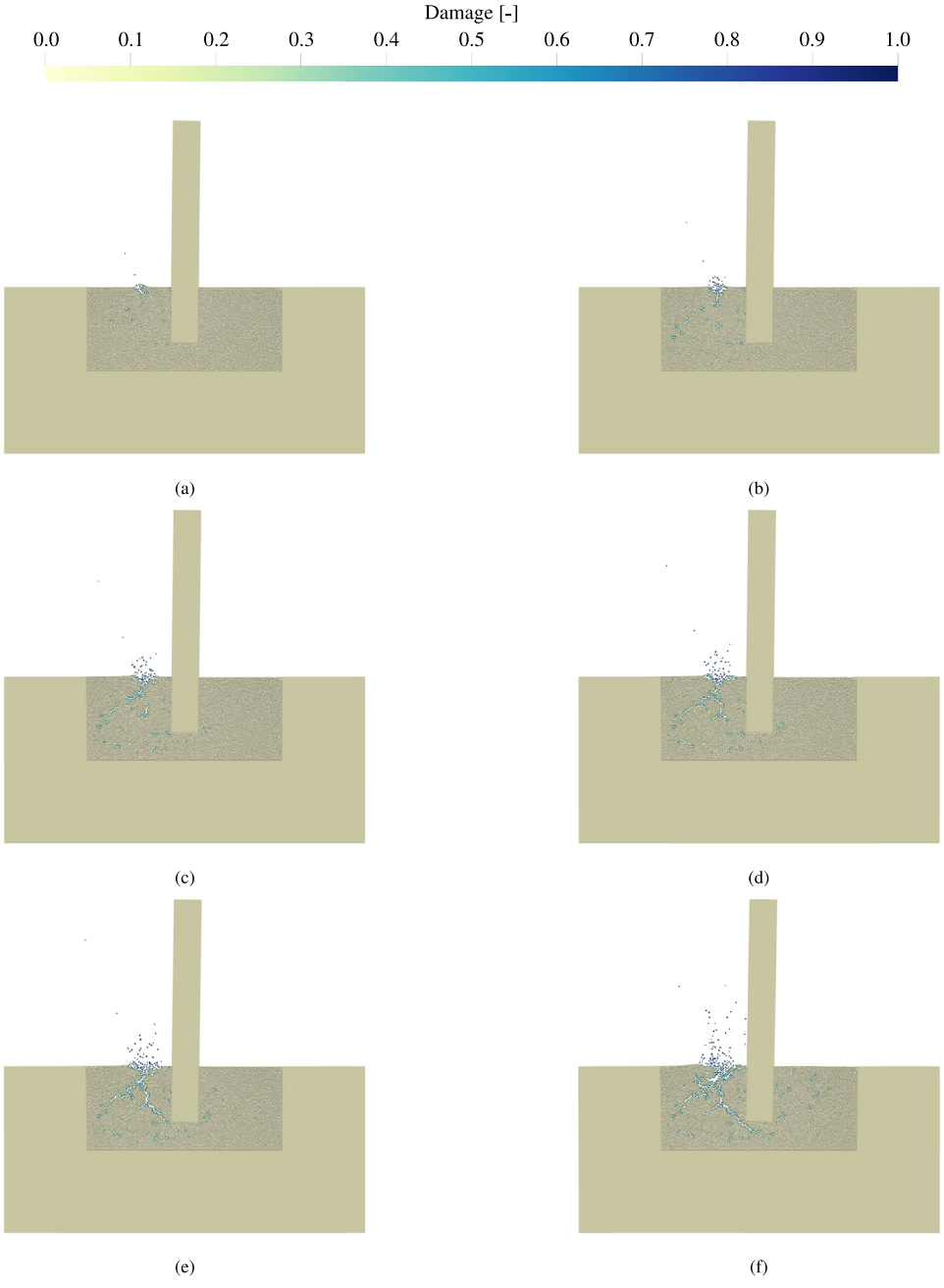

Fig. 24. Damage propagation at: (a) 42 ms, (b) 47 ms, (c) 52 ms, (d) 55 ms, (e) 57 ms, (f) 67 ms. Displacements are exaggerated by a factor of 5. See Appendix online version for the video.

damping via viscoelasticity and simulations involving poroelasticity. It should also be mentioned that the coupling technique presented in this work is generic enough to allow other discrete methods to be coupled with the BEM.

Declaration of competing interest

The authors declare the following financial interests/personal relationships which may be considered as potential competing interests: Klaus Thoeni and Jerzy Rojek reports financial support was provided by Australian Research Council.

Data availability

No data was used for the research described in the article.

Acknowledgements

The authors would like to acknowledge the financial support of the Australian Research Council, Australia (DP190102407).

Appendix A. Supplementary data

Supplementary material related to this article can be found online at https://doi.org/10.1016/j.cma.2023.116227.

References

[1] M. Jiang, Y. Dai, L. Cui, Z. Shen, X. Wang, Investigating mechanism of inclined CPT in granular ground using DEM, Granul. Matter 16 (2014) 785–796.
[2] Y. Ma, H. Huang, DEM analysis of failure mechanisms in the intact Brazilian test, Int. J. Rock Mech. Min. Sci. 102 (2018) 109–119.
[3] J.S. Vinod, DEM simulations in geotechnical earthquake engineering education, Int. J. Geotech. Earthq. Eng. 1 (2010) 61–69.
[4] M. Panji, B. Ansari, Transient SH-wave scattering by the lined tunnels embedded in an elastic half-plane, Eng. Anal. Bound. Elem. 84 (2017) 220–230.
[5] M. Omidvar, M. Iskander, S. Bless, Response of granular media to rapid penetration, Int. J. Impact Eng. 66 (2014) 60–82.
[6] F. Donzé, J. Bouchez, S. Magnier, Modeling fractures in rock blasting, Int. J. Rock Mech. Min. Sci. 34 (1997) 1153–1163.
[7] A. Fakhimi, M. Lanari, DEM–SPH simulation of rock blasting, Comput. Geotech. 55 (2014) 158–164.
[8] B. Regassa, N. Xu, G. Mei, An equivalent discontinuous modeling method of jointed rock masses for DEM simulation of mining-induced rock movements, Int. J. Rock Mech. Min. Sci. 108 (2018) 1–14.
[9] C. Labra, J. Rojek, E. Oñate, F. Zarate, Advances in discrete element modelling of underground excavations, Acta Geotech. 3 (2008) 317–322.
[10] G. Beer, B. Marussig, C. Duenser, Isogeometric boundary element method for the simulation of underground excavations, Géotech. Lett. 3 (2013) 108–111.
[11] J. Rojek, E. Oñate, C. Labra, H. Kargl, Discrete element simulation of rock cutting, Int. J. Rock Mech. Min. Sci. 48 (2011) 996–1010.
[12] B. Marco, P. Giovanna, G. Giovanni, Rock slide simulation with the combined finite-discrete element method, Int. J. Geomech. 12 (2012) 711–721.
[13] Z. Nie, Z. Zhang, H. Zheng, Slope stability analysis using convergent strength reduction method, Eng. Anal. Bound. Elem. 108 (2019) 402–410.
[14] H.K. Dang, M.A. Meguid, An efficient finite-discrete element method for quasi-static nonlinear soil-structure interaction problems, Int. J. Numer. Anal. Methods Geomech. 37 (2) (2013) 130–149, http://dx.doi.org/10.1002/nag.1089.
[15] W. Moser, H. Antes, G. Beer, Soil-structure interaction and wave propagation problems in 2D by a duhamel integral based approach and the convolution quadrature method, Comput. Mech. 36 (2005) 431–443.
[16] R.P. Chen, L.J. Tang, D.S. Ling, Y.M. Chen, Face stability analysis of shallow shield tunnels in dry sandy ground using the discrete element method, Comput. Geotech. 38 (2011) 187–195.
[17] G. Beer, J.O. Watson, G. Swoboda, Three-dimensional analysis of tunnels using infinite boundary elements, Comput. Geotech. 3 (1987) 37–58.
[18] M. Panji, H. Koohsari, M. Adampira, H. Alielahi, J.A. Marnani, Stability analysis of shallow tunnels subjected to eccentric loads by a boundary element method, J. Rock Mech. Geotech. Eng. 8 (2016) 480–488.
[19] C.C. Spyrakos, D.E. Beskos, Dynamic response of rigid strip-foundations by a time-domain boundary element method, Int. J. Numer. Methods Eng. 23 (1986) 1547–1565.
[20] J. Lemos, Discrete element analysis of dam foundations, in: Distinct Element Modelling in Geomechanics, Routledge, 2018, pp. 89–115.
[21] A.A. Bandeira, T.I. Zohdi, 3D numerical simulations of granular materials using DEM models considering rolling phenomena, Comput. Part. Mech. 6 (2019) 97–131.
[22] P.A. Cundall, O.D.L. Strack, A discrete numerical model for granular assemblies, Géotechnique 29 (1979) 47–65.
[23] D.O. Potyondy, P.A. Cundall, A bonded-particle model for rock, Int. J. Rock Mech. Min. Sci. 41 (2004) 1329–1364.

[24] D. Song, X. Quan, M. Liu, C. Liu, W. Liu, X. Wang, D. Han, Investigation on the seismic wave propagation characteristics excited by explosion source in high-steep rock slope site using discrete element method, Sustainability 14 (2022) 17028.
[25] Z. You, W. Lord, Elastic wave propagation in an infinite media, in: D.O. Thompson, D.E. Chimenti (Eds.), Review of Progress in Quantitative Nondestructive Evaluation, Springer US, Boston, MA, 1990, pp. 133–140.
[26] Y. Heider, W. Markert, Dynamic wave propagation in infinite saturated porous media half spaces, Comput. Mech. 49 (2012) 319–336.
[27] G. Beer, J.O. Watson, Infinite boundary elements, Int. J. Numer. Methods Eng. 28 (1989) 1233–1247.
[28] C.A. Brebbia, J.C.F. Telles, L.C. Wrobel, Boundary Elements Techniques, Springer-Verlag, Berlin Heidelberg, 1984.
[29] W.J. Mansur, C.A. Brebbia, Formulation of the boundary element method for transient problems governed by the scalar wave equation, Appl. Math. Model. 6 (1982) 307–311.
[30] J. Dominguez, Boundary Elements in Dynamics, Elsevier Applied Science, London, 1993, p. 450.
[31] M. Schanz, Wave Propagation in Viscoelastic and Poroelastic Continua: A Boundary Element Approach, Springer-Verlag, Berlin, 2001.
[32] C. Lubich, Convolution quadrature and discretized operational calculus. I, Numer. Math. 52 (1988) 129–145.
[33] T. Zohdi, Computation of strongly coupled multifield interaction in particle–fluid systems, Comput. Methods Appl. Mech. Eng. 196 (2007) 3927–3950.
[34] C. Labra, J. Rojek, E. Oñate, Discrete/finite element modelling of rock cutting with a TBM disc cutter, Rock Mech. Rock Eng. 50 (2017) 621–638.
[35] M. Lak, M. Fatehi Marji, A. Yarahmadi Bafghi, A. Abdollahipour, A coupled finite difference-boundary element method for modeling the propagation of explosion-induced radial cracks around a wellbore, J. Nat. Gas Sci. Eng. 64 (2019) 41–51.
[36] E. Oñate, J. Rojek, Combination of discrete element and finite element methods for dynamic analysis of geomechanics problems, Comput. Methods Appl. Mech. Eng. 193 (2004) 3087–3128.
[37] N.M. Azevedo, J.V. Lemos, Hybrid discrete element/finite element method for fracture analysis, Comput. Methods Appl. Mech. Eng. 195 (2006) 4579–4593.
[38] J. Rojek, E. Oñate, Multiscale analysis using a coupled discrete/finite element model, Interact. Multiscale Mech. 1 (2008) 1–31.
[39] S.P. Xiao, T. Belytschko, A bridging domain method for coupling continua with molecular dynamics, Comput. Methods Appl. Mech. Eng. 193 (2004) 1645–1669.
[40] P.T. Bauman, H.B. Dhia, N. Elkhodja, J.T. Oden, S. Prudhomme, On the application of the arlequin method to the coupling of particle and continuum models, Comput. Mech. 42 (2008) 511–530.
[41] J. Rousseau, E. Frangin, P. Marin, L. Daudeville, Multidomain finite and discrete elements method for impact analysis of a concrete structure, Eng. Struct. 31 (2009) 2735–2743.
[42] X. Li, K. Wan, A bridging scale method for granular materials with discrete particle assembly - cosserat continuum modeling, Comput. Geotech. 38 (2011) 1052–1068.
[43] F. Zárate, E. Oñate, A simple FEM–DEM technique for fracture prediction in materials and structures, Comput. Part. Mech. 2 (2015) 301–314.
[44] F. Zárate, A. Cornejo, E. Oñate, A three-dimensional FEM–DEM technique for predicting the evolution of fracture in geomaterials and concrete, Comput. Part. Mech. 5 (2018) 411–420.
[45] A. Cornejo, V. Mataix, F. Zárate, E. Oñate, Combination of an adaptive remeshing technique with a coupled FEM–DEM approach for analysis of crack propagation problems, Comput. Part. Mech. 7 (2020) 735–752.
[46] O.C. Zienkiewicz, D.W. Kelly, P. Bettess, The coupling of the finite element method and boundary solution procedures, Int. J. Numer. Methods Eng. 11 (1977) 355–375.
[47] C. Brebbia, P. Georgiou, Combination of boundary and finite elements in elastostatics, Appl. Math. Model. 3 (1979) 212–220.
[48] G. Beer, Finite element, boundary element and coupled analysis of unbounded problems in elastostatics, Int. J. Numer. Methods Eng. 19 (1983) 567–580.
[49] O. von Estorff, M.J. Prabucki, Dynamic response in the time domain by coupled boundary and finite elements, Comput. Mech. 6 (1990) 35–46.
[50] D. Soares, W.J. Mansur, O.V. Estorff, An efficient time-domain FEM/BEM coupling approach based on FEM implicit Green's functions and truncation of BEM time convolution process, Comput. Methods Appl. Mech. Eng. 196 (2007) 1816–1826.
[51] T. Rüberg, M. Schanz, Coupling finite and boundary element methods for static and dynamic elastic problems with non-conforming interfaces, Comput. Methods Appl. Mech. Eng. 198 (2008) 449–458.
[52] S. François, P. Coulier, G. Degrande, Finite element–boundary element coupling algorithms for transient elastodynamics, Eng. Anal. Bound. Elem. 55 (2015) 104–121.
[53] T. Burczynski, A. Mrozek, W. Kuś, A computational continuum-discrete model of materials, Bull. Polish Acad. Sci.-Tech. Sci. 55 (2007) 85–89.
[54] M. Mirzayee, N. Khaji, M. Ahmadi, A hybrid distinct element–boundary element approach for seismic analysis of cracked concrete gravity dam–reservoir systems, Soil Dynam. Earthq. Eng. 31 (2011) 1347–1356.
[55] L.J. Lorig, B.H.G. Brady, P.A. Cundall, Hybrid distinct element-boundary element analysis of jointed rock, Int. J. Rock Mech. Min. Sci. 23 (1986) 303–312.
[56] A.-B. Huang, M.Y. Ma, J.S. Lee, A micromechanical study of penetration tests in granular material, Mech. Mater. 16 (1993) 133–139.
[57] L. Malinowski, G.F. Karlis, G. Beer, J. Rojek, Iterative coupling of boundary and discrete element methods using an overlapping FEM zone, in: COUPLED IV: Proceedings of the IV International Conference on Computational Methods for Coupled Problems in Science and Engineering, CIMNE, 2011, pp. 301–312.
[58] G. Barros, A. Pereira, J. Rojek, K. Thoeni, DEM-BEM coupling in time domain for one-dimensional wave propagation, Eng. Anal. Bound. Elem. 135 (2022) 26–37.

[59] G. Barros, V. Sapucaia, P. Hartmann, A. Pereira, J. Rojek, K. Thoeni, A novel BEM-DEM coupling in the time domain for simulating dynamic problems in continuous and discontinuous media, Comput. Methods Appl. Mech. Engrg. 410 (2023) 116040.
[60] V. Smilauer, V. Angelidakis, E. Catalano, R. Caulk, B. Chareyre, W. Chèvremont, S. Dorofeenko, J. Duriez, N. Dyck, J. Elias, B. Er, A. Eulitz, A. Gladky, N. Guo, C. Jakob, F. Kneib, J. Kozicki, D. Marzougui, R. Maurin, C. Modenese, G. Pekmezi, L. Scholtès, L. Sibille, J. Stransky, T. Sweijen, K. Thoeni, C. Yuan, Yade Documentation, The Yade Project, 2021, http://dx.doi.org/10.5281/zenodo.5705394.
[61] C. O'Sullivan, Particulate Discrete Element Modelling: A Geomechanics Perspective, CRC Press, 2011.
[62] L. Verlet, Computer "experiments" on classical fluids. I. Thermodynamical properties of Lennard-Jones molecules, Phys. Rev. 159 (1967) 98–103.
[63] B. Chareyre, P. Villard, Dynamic spar elements and discrete element methods in two dimensions for the modeling of soil-inclusion problems, J. Eng. Mech. 131 (2005) 689–698.
[64] R. Hosn, L. Sibille, N. Benahmed, B. Chareyre, Discrete numerical modeling of loose soil with spherical particles and interparticle rolling friction, Granul. Matter 19 (2017) 1–12.
[65] A. Cornejo, A. Franci, F. Zárate, E. Oñate, A fully Lagrangian formulation for fluid-structure interaction problems with free-surface flows and fracturing solids, Comput. Struct. 250 (2021) 106532.
[66] J. Carter, J. Booker, Sudden excavation of a long circular tunnel in elastic ground, Int. J. Rock Mech. Min. Sci. Geomech. Abstracts 27 (1990) 129–132.
[67] J.R. Shewchuk, Triangle: Engineering a 2D quality mesh generator and delaunay triangulator, in: M.C. Lin, D. Manocha (Eds.), Applied Computational Geometry Towards Geometric Engineering, 1996, pp. 203–222.